Sensitivity of ORCA to the neutrino mass hierarchy

Bachelorarbeit aus der Physik

vorgelegt von
Steffen Hallmann

4. April 2013

Erlangen Centre for Astroparticle Physics
Physikalisches Institut
Friedrich-Alexander-Universität Erlangen-Nürnberg

1. Gutachter: Prof. Dr. Gisela Anton
2. Gutachter: Dr. Jürgen Hößl

ERLANGEN CENTRE FOR ASTROPARTICLE PHYSICS

ORCA KM3NeT

Abstract

Recent measurements have shown that the value of the neutrino mixing angle θ_{13} is surprisingly large. Due to matter effects in the Earth, this may lead to a measurable difference between the rates of atmospheric neutrinos for normal and inverted mass hierarchy. Feasibility studies on the determination of the neutrino mass hierarchy with megaton-scale water and ice Cherenkov detectors are therefore underway.

In this thesis, the expected rates of atmospheric muon neutrino interactions are calculated for ORCA, a first phase option for the future KM3NeT detector in the Mediterranean Sea. The statistical asymmetry of neutrino rates between normal and inverted mass hierarchy is shown. To estimate the measuring times needed to determine the neutrino mass hierarchies for different detector resolutions, a binned log-likelihood ratio test is used. Finally, the influences of uncertainties of the neutrino oscillation parameters on the mass hierarchy measurement are analysed.

Contents

1. Neutrino oscillations in vacuum and the neutrino mass hierarchy problem

Oscillation experiments with solar and atmospheric neutrinos have shown that neutrinos are massive and that their flavour eigenstates differ from their mass eigenstates. Flavour eigenstates ν_α ($\alpha = e, \mu, \tau$), taking part in weak interactions, are linear combinations of the mass eigenstates ν_i ($i = 1, 2, 3$), controlling free particle evolution. In vacuum, they are related by the unitary PMNS mixing matrix $\mathcal{U}$:[1]

$$\begin{aligned}\begin{pmatrix}\nu_e\\ \nu_\mu\\ \nu_\tau\end{pmatrix} &= \mathcal{U} \times \begin{pmatrix}\nu_1\\ \nu_2\\ \nu_3\end{pmatrix} \\ &= \begin{pmatrix}1 & 0 & 0\\ 0 & \mathrm{c}_{23} & \mathrm{s}_{23}\\ 0 & -\mathrm{s}_{23} & \mathrm{c}_{23}\end{pmatrix} \begin{pmatrix}\mathrm{c}_{13} & 0 & \mathrm{s}_{13}e^{-i\delta}\\ 0 & 1 & 0\\ -\mathrm{s}_{13}e^{-i\delta} & 0 & \mathrm{c}_{13}\end{pmatrix} \begin{pmatrix}\mathrm{c}_{12} & \mathrm{s}_{12} & 0\\ -\mathrm{s}_{12} & \mathrm{c}_{12} & 0\\ 0 & 0 & 1\end{pmatrix} \begin{pmatrix}\nu_1\\ \nu_2\\ \nu_3\end{pmatrix}.\end{aligned} \tag{1}$$

Here, the two Majorana phases are neglected, since they have no effect on oscillation experiments. In this notation c_{ij} and s_{ij} is short for the cosine and the sine of the mixing angle θ_{ij}, $\cos\theta_{ij}$ and $\sin\theta_{ij}$. The time evolution in the mass basis and flavour basis is given by the Schrödinger Equation:

$$i\frac{\mathrm{d}}{\mathrm{d}t}\begin{pmatrix}\nu_1(t)\\ \nu_2(t)\\ \nu_3(t)\end{pmatrix} = \mathcal{H}_0 \begin{pmatrix}\nu_1(t)\\ \nu_2(t)\\ \nu_3(t)\end{pmatrix}, \qquad i\frac{\mathrm{d}}{\mathrm{d}t}\begin{pmatrix}\nu_e(t)\\ \nu_\mu(t)\\ \nu_\tau(t)\end{pmatrix} = \mathcal{H}_0^f \begin{pmatrix}\nu_e(t)\\ \nu_\mu(t)\\ \nu_\tau(t)\end{pmatrix}. \tag{2}$$

In vacuum the Hamiltonian $\mathcal{H}_0$ in the mass basis is diagonal

$$\mathcal{H}_0 = \begin{pmatrix}E_1 & 0 & 0\\ 0 & E_2 & 0\\ 0 & 0 & E_3\end{pmatrix}, \qquad E_i = \sqrt{m_i^2 + \boldsymbol{p}^2}. \tag{3}$$

The solution to the time evolution of flavour states in vacuum can then be written as a unitary transformation U_f

$$\begin{pmatrix}\nu_e(t)\\ \nu_\mu(t)\\ \nu_\tau(t)\end{pmatrix} = U_f \begin{pmatrix}\nu_e(0)\\ \nu_\mu(0)\\ \nu_\tau(0)\end{pmatrix} = e^{-i\mathcal{H}_0^f t} \begin{pmatrix}\nu_e(0)\\ \nu_\mu(0)\\ \nu_\tau(0)\end{pmatrix} = \mathcal{U}e^{-i\mathcal{H}_0 t}\mathcal{U}^{-1} \begin{pmatrix}\nu_e(0)\\ \nu_\mu(0)\\ \nu_\tau(0)\end{pmatrix} \tag{4}$$

The transition probabilities between two flavours – measured by neutrino oscillation experiments – are then just the square of the transition amplitudes $\psi_{\alpha\beta}(t)$ from flavour state ν_α to ν_β after a time t:

$$P_{\nu_\alpha \to \nu_\beta}(t) = |\psi_{\alpha\beta}(t)|^2 = |\langle \nu_\beta | \nu_\alpha(t) \rangle|^2 \tag{5}$$

[1] The formulae for neutrino oscillations in vacuum and matter follow [1], [2] and [3, c. 13].

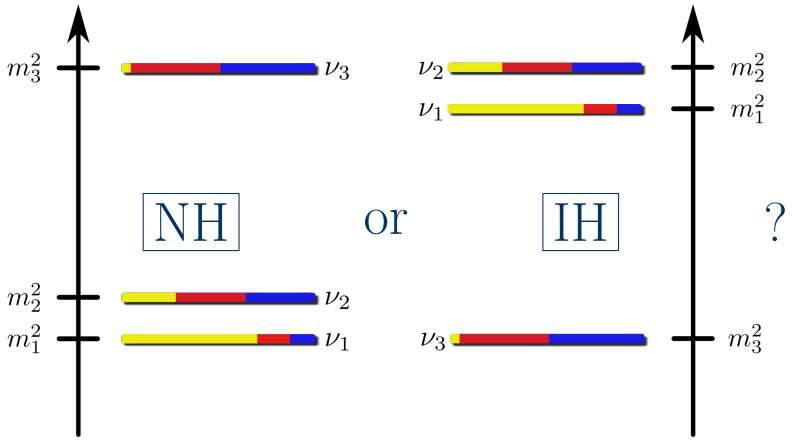

Figure 1: Normal (NH) and inverted (IH) mass hierarchy as possible ways to order neutrino masses. Figure adapted from [5]

Calculating these using the equations above and for ultrarelativistic neutrinos substituting

$$E_i \approx E_\nu + \frac{m_i^2}{2E_\nu}, \qquad \boldsymbol{p} \approx E_\nu, \qquad t \approx L \tag{6}$$

yields the transition probabilities in vacuum. In addition to the mixing angles and the CP violating phase in the PMNS matrix (see Eq. 1) they depend on squared mass differences between the mass eigenstates $\Delta m_{ij}^2 = m_i^2 - m_j^2$, the distance from source to detector L and neutrino energy E_ν.

Matter effects in the sun [4, and references therein] allow experiments with solar neutrinos to measure the sign of the mass splitting between the first and the second mass eigenstate $\delta m^2 = \Delta m_{21}^2$, while for the much larger atmospheric mass splitting only the absolute value can be determined $\left|\Delta m^2\right| = \left|m_3^2 - (m_1^2 + m_2^2)/2\right| \approx \left|\Delta m_{31}^2\right| \approx \left|\Delta m_{32}^2\right|$. Knowing that $m_1 < m_2$ there are two remaining possibilities to order neutrino masses, named normal hierarchy (NH) for $m_1 < m_2 < m_3$ and inverted hierarchy (IH) for $m_3 < m_1 < m_2$ as depicted in Fig. 1.

Since the absolute value of neutrino masses and the existence of Majorana phases cannot be determined by oscillation experiments, there are two unknown neutrino properties that can possibly be determined by oscillation experiments: The CP violating phase δ_{CP} and the sign of the large mass difference Δm^2.

The recent discovery of a suprisingly large θ_{13} mixing angle [6][7] has drawn attention to the determination of the neutrino mass hierarchy (MH).

The possibility to use atmospheric neutrinos with an energy of 1–20 GeV for an energy and zenith angle dependent measurement was shown [8] as an inexpensive alternative to long baseline accelerator experiments. Therefore feasibility studies on the MH determination are underway for large scale Cherenkov detectors in water and ice. The possibility

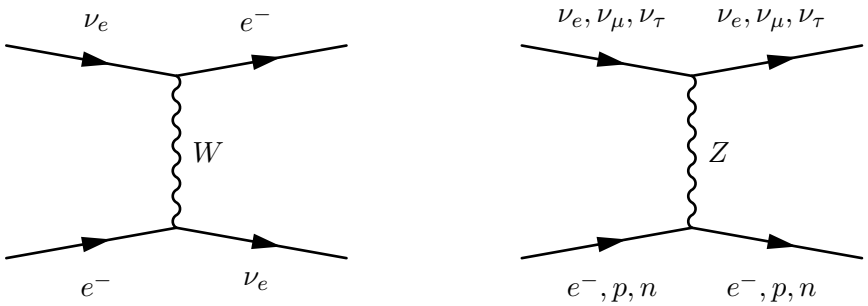

Figure 2: Feynman diagrams for coherent weak forward scattering involving a $W^\pm$ for CC (left) and a Z for NC (right)

to reconstruct neutrinos with energies as low as 20 GeV even with ANTARES, a neutrino detector in the Mediterranean Sea designed for high energy neutrino signals, has recently been shown [9]. Due to the priority of a MH measurement, a dedicated feasibility study named ORCA "**O**scillation **R**esearch with **C**osmics in the **A**byss" is run as a phase I option for the KM3NeT detector, a future multi-megaton water Cherenkov detector in the Mediterranean Sea.

The outline for this thesis is as follows. In the next section, Sec. 2, matter effects on neutrino oscillations will be discussed. In Sec. 3, the journey of atmospheric neutrinos is accompanied from production and oscillation in the Earth to interaction and identification in the detector. These form the ingredients to calculate muon neutrino rates and the asymmetry between NH and IH in Sec. 4. Section 5 will take into account the consequences of the transition from neutrino to muon on the distribution of measured events. A log-likelihood estimate to get the probability value (p-value) to exclude either NH or IH is introduced in Sec. 6 and the p-value is subsequently calculated for different scenarios of detector resolution in Sec. 7. Finally, in Sec. 8, the effects of uncertainties of the neutrino parameters on the measurement are elaborated before the main results are resumed in Sec. 9.

2. Neutrino oscillations in matter

In matter, an additional potential arises for neutrinos due to coherent weak forward scattering on electrons and nucleons in matter [1]. The neutral current potential, shown in Fig. 2, is equal for all types of neutrinos (and thus yields just an additional phase identical for all neutrino types), whereas the charged current (CC) potential only affects electron flavour neutrinos. The CC potential adds an additional interaction term $\mathcal{H}_I^f$ to the vacuum Hamiltonian in the flavour basis, which in the 3 neutrino framework is:

$$\mathcal{H}_I^f = \pm V_{CC} \begin{pmatrix} 1 & 0 & 0 \\ 0 & 0 & 0 \\ 0 & 0 & 0 \end{pmatrix} = \pm\sqrt{2} G_F N_e \begin{pmatrix} 1 & 0 & 0 \\ 0 & 0 & 0 \\ 0 & 0 & 0 \end{pmatrix}, \tag{7}$$

where G_F is the Fermi coupling constant and N_e the electron number density. The positive (negative) sign applies to neutrinos (antineutrinos).

The effect of this interaction term $\mathcal{H}_I^f$ is that the total Hamiltonian $\mathcal{H}_{tot}^f = \mathcal{H}_0^f + \mathcal{H}_I^f = \mathcal{U}\,\mathcal{H}_0\,\mathcal{U}^{-1} + \mathcal{H}_I^f$ is diagonal neither in the flavour nor in the mass eigenstate basis. Thus also $\nu_i \leftrightarrow \nu_j$ $(i, j = 1, 2, 3)$ transitions are allowed.

The major effect of the additional matter potential is that the squared mass differences in matter are shifted with respect to those in vacuum. For the electron number densities present in the Earth and neutrino energies $E_\nu \gtrsim 2\,\mathrm{GeV}$ the effect is, to good approximation, negligible for the small mass difference δm^2 [3, c. 13]. Thus, to see the consequences for neutrino oscillations, the problem can for simplicity be reduced to a two neutrino mixing between the first and the third mass eigenstate.

In presence of matter, the mass difference in vacuum changes into an effective mass difference $\Delta m^2_{13\,\mathrm{eff}}$:

$$\Delta m^2_{13\,\mathrm{eff}} = \Delta m^2_{13}\sqrt{\left(\cos(2\theta_{13}) - A\right)^2 + \sin^2(2\theta_{13})} \tag{8}$$

with

$$A = \pm\frac{2\sqrt{2}G_F N_e E_\nu}{\Delta m^2_{13}} \tag{9}$$

with positive (negative) sign for neutrinos (antineutrinos).

Also, the mixing angle θ_{13} is converted into an effective mixing angle:

$$\tan\left(2\theta_{13}^{\mathrm{eff}}\right) = \frac{\tan\left(2\theta_{13}\right)}{1 - \frac{A}{\cos(2\theta_{13})}} \tag{10}$$

Mikheyev, Smirnov and Wolfenstein [10][11] found that this gives rise to a resonance in matter for

$$A = \cos(2\theta_{13}), \tag{11}$$

where the mixing can become maximal even if the vacuum mixing angle θ_{13} is small (MSW effect). Note, that in the limit of small electron number densities $N_e \approx 0$ the vacuum values for θ_{13} and Δm^2_{13} are retrieved.

Inserting Eq. 9 into Eq. 11, the resonance condition in terms of neutrino energy is

$$E_\nu^{\mathrm{res}} = \pm\frac{\Delta m^2_{13}\cos(2\theta_{13})}{2\sqrt{2}G_F N_e}. \tag{12}$$

It can be seen that the resonance condition can be fulfilled for neutrinos only in the case of normal hierarchy ("+" and positive Δm^2_{13}) and for antineutrinos only in the case of inverted hierarchy ("−" and negative Δm^2_{13}). Thus, the effects of matter on the oscillation probabilities are different for NH compared to IH.

For the Earth, the average electron number densities are $\overline{N}_e^{\mathrm{core}} \approx 5.4\,\mathrm{cm}^{-3} \cdot N_A$ in the core and $\overline{N}_e^{\mathrm{mantle}} \approx 2.2\,\mathrm{cm}^{-3} \cdot N_A$ in the mantle [12], with Avogadro's number N_A. Hence, using Eq. 12, the resonance energies are $E_{\nu,\,\mathrm{res}}^{\mathrm{core}} \approx 3\,\mathrm{GeV}$ for the core and $E_{\nu,\,\mathrm{res}}^{\mathrm{mantle}} \approx 7\,\mathrm{GeV}$ for the mantle.

Given abrupt periodical changes in matter density, the mixing can be enhanced although the matter density is not at the resonance value. This affects neutrinos travelling through the Earth since the core is much denser than the mantle. This phenomenon is known as "parametric enhancement" and an explanation can be found in Ref. [13].

In the following, the rates of atmospheric neutrinos at the detector will be calculated. As shown, matter effects on neutrino oscillations are different for NH and IH. Rates will therefore depend on the neutrino mass hierarchy.

3. Atmospheric neutrinos: from production to detection

3.1. Atmospheric neutrino flux

The Earth is permanently hit by high energy cosmic radiation, predominantly protons, which are mainly produced outside the solar system. Supernovae explosions have recently been identified as an origin of cosmic radiation [14]. Since they are deflected by interstellar magnetic fields, the flux of primary cosmic rays approaching the Earth is, to good approximation, isotropically distributed [15]. In interactions with nuclei in the atmosphere both hadronic and electromagnetic showers are produced. In these showers atmospheric neutrinos are mainly created in charged pion and kaon decays [3]

$$\begin{aligned} \pi^- &\longrightarrow \mu^- \, \overline{\nu}_\mu \longrightarrow e^- \, \overline{\nu}_e \, \nu_\mu \, \overline{\nu}_\mu && \text{(accordingly for } \pi^+\text{)} \\ K^- &\longrightarrow \pi^- \pi^0 && \text{(accordingly for } K^+\text{)} \\ &\longrightarrow \mu^- \, \overline{\nu}_\mu \longrightarrow e^- \, \overline{\nu}_e \, \nu_\mu \, \overline{\nu}_\mu \end{aligned}$$

leading to a $(\nu_\mu + \overline{\nu}_\mu)/(\nu_e + \overline{\nu}_e)$ ratio of ≈ 2.

If neutrinos were not subject to neutrino oscillation, the atmospheric flux for each flavour was, to first order, up-down symmetric as a consequence of the isotropic distribution of primary particles [15]. This is because the atmospheric neutrino flux traverses Earth without appreciable attenuation due to the long mean free path of neutrinos in matter.

For a MH measurement, flux calcutations of neutrinos with energies of a few GeV are needed. This is where low energy primaries start to contribute to the rate that (a) originate from the sun and (b) have low enough rigidity (= momentum/charge) to be influenced by the geomagnetic field. This has two main consequences: (→a) The level of proton flux from the sun is modulated by the solar cycle and is higher for solar maximum than for solar minimum and (→b) low energy cosmic rays cannot permeate the geomagnetic field from all directions ("rigidity cut-off"), which necessitates a 3-dimensional calculation to account for geomagnetism [15].

The three independent flux calculations usually considered are HKKM [16], Bartol [17] and FLUKA [18]. Above 5 GeV the shapes of the angular and energy dependences of the three models agree at the 5% level. The overall amplitude of HKKM and Bartol agrees at the level of a few percents, whereas the FLUKA model differs from the others by more than 20% [19].

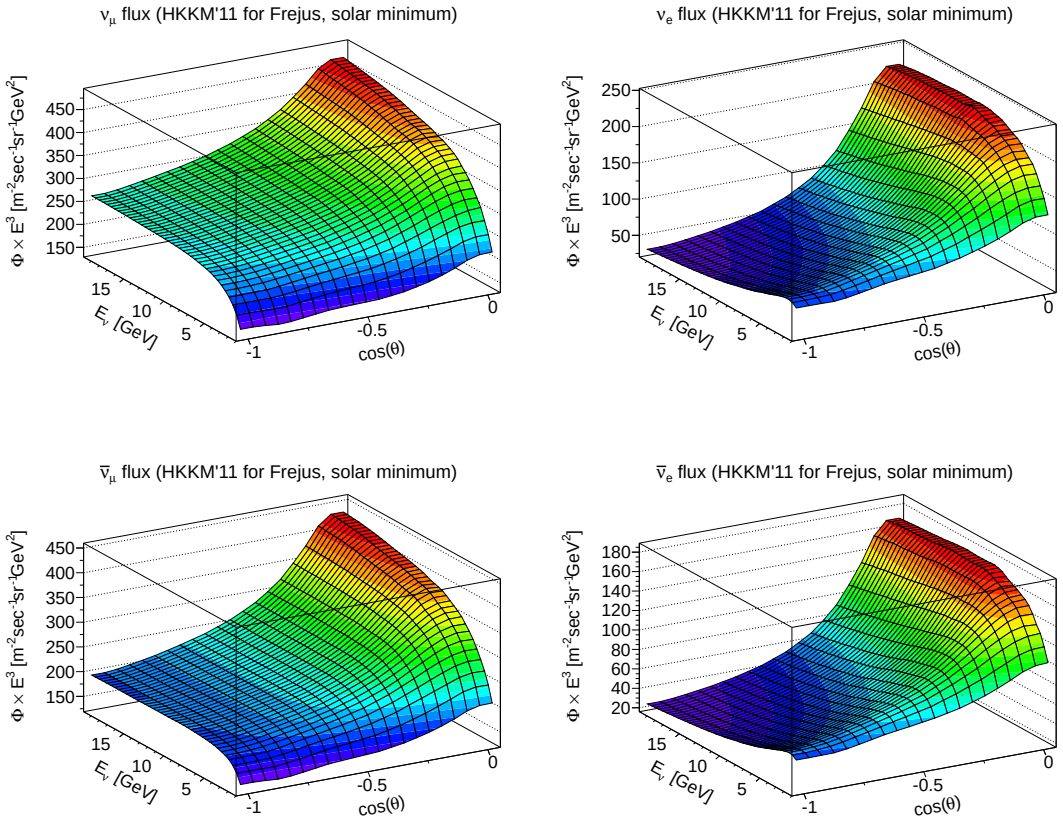

Figure 3: Interpolated HKKM'11 [20] fluxes Φ for ν_μ (top left), ν_e (top right), $\overline{\nu}_\mu$ (bottom left) and $\overline{\nu}_e$ (bottom right).

This work takes the azimuth averaged HKKM'11 flux [20] calculated for solar minimum. An explicit flux calculation for (42° 47.935′ N, 6° 09.942′ E) as one of the envisaged sites for the ORCA detector is not available in near-term. Therefore the calculation for the nearby Frejus site is used for ORCA.[2]

For up-going muon and electron (anti)neutrinos, the interpolated HKKM'11 fluxes of up-going neutrinos are depicted in Fig. 3. Note that the antineutrino rates are only $\approx 75\%$ of the neutrino rates.

3.2. Neutrino oscillations in the Earth

The theory of neutrino oscillation in matter has already been introduced in Sec. 2. Probabilities for transitions between the three different flavours ν_e, ν_μ and ν_τ have been calculated numerically [22] for neutrinos and antineutrinos.

[2] At least for the site (42° 47.935′ N, 6° 09.942′ E) , the fluxes calculated for Frejus are most conform to the fluxes for ORCA. Regarding the geomagnetic cut-off, they are in particular more appropriate than the fluxes calculated for the also nearby Gran Sasso site.[21]

Table 1: Global best fit values for the different neutrino oscillation parameters, taken from [23].

Parameter	Best fit	1σ range
$\delta m^2/10^{-5}\,\mathrm{eV}^2$ (NH or IH)	7.54	7.32 – 7.80
$\sin^2\theta_{12}/10^{-1}$ (NH or IH)	3.07	2.91 – 3.25
$\Delta m^2/10^{-3}\,\mathrm{eV}^2$ (NH)	2.43	2.33 – 2.49
$\Delta m^2/10^{-3}\,\mathrm{eV}^2$ (IH)	2.42	2.31 – 2.49
$\sin^2\theta_{13}/10^{-2}$ (NH)	2.41	2.16 – 2.66
$\sin^2\theta_{13}/10^{-2}$ (IH)	2.44	2.19 – 2.67
$\sin^2\theta_{23}/10^{-1}$ (NH)	3.86	3.65 – 4.10
$\sin^2\theta_{23}/10^{-1}$ (IH)	3.92	3.70 – 4.31
δ/π (NH)	1.08	0.77 – 1.36
δ/π (IH)	1.09	0.83 – 1.47

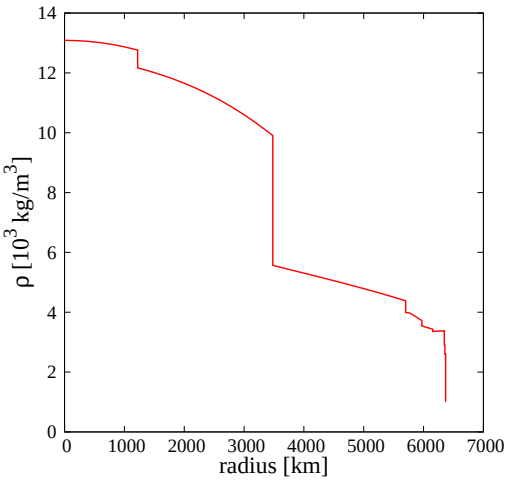

Figure 4: Earth density profile according to the PREM model [12].

As an input to this calculation of oscillation probabilities, the neutrino parameters were taken from the most recent global fit [23] and are tabulated in Tab. 1. The PREM [12] parametrisation was used for the matter distribution inside the Earth (see Fig. 4). Density changes abruptly from $\rho = 5.6 \times 10^3\,\mathrm{kg/m}^3$ to $\rho = 9.9 \times 10^3\,\mathrm{kg/m}^3$ at a radius of 3,480 km. This is the transition from the outer core to the mantle. At the detector, neutrinos with the cosine of the zenith angle $\cos(\theta_z^\nu) \lesssim -0.83$ have traversed the core, which is visible in the oscillation probability histograms in Fig. 5.

In the limit $\delta m^2 \to 0$ oscillation probabilities for ν_μ and $\overline{\nu}_\mu$ are swapped for NH with respect to IH [8]. Since δm^2 is small, this effect can also be seen by comparing the NH

(IH) ν_μ histograms with the IH (NH) $\overline{\nu}_\mu$ histograms given in Appendix B. Hence, if the direction and energy dependent number of detected neutrinos were the same as the number of antineutrinos a MH determination would be impossible. Fortunately, both fluxes and cross sections are higher for neutrinos compared to antineutrinos.

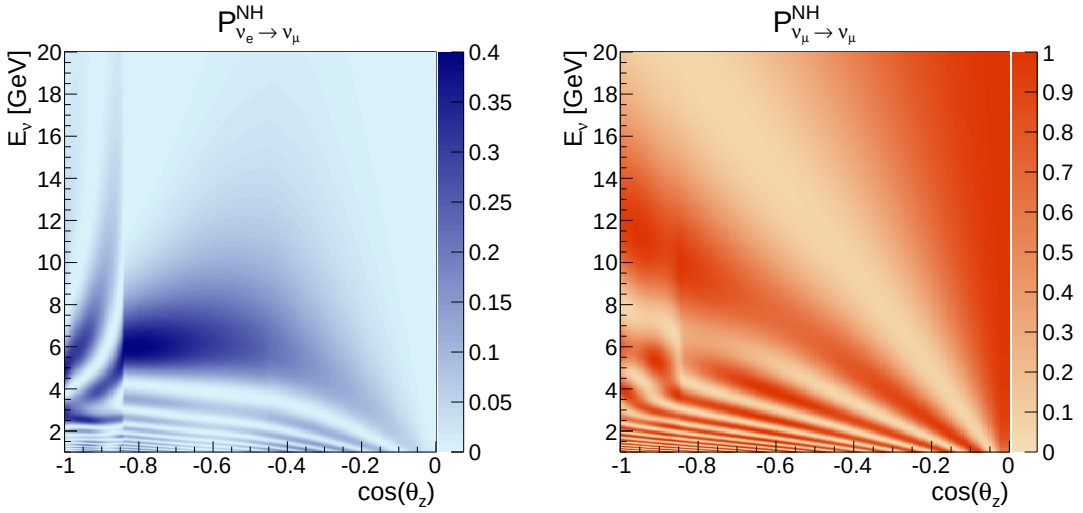

Figure 5: Appearance and survival probabilities for ν_μ , assuming normal hierarchy.

3.3. Charged current cross sections

In large volume water and ice detectors, charged particles are detected through the Cherenkov light they emit when travelling at speeds exceeding the speed of light in the respective medium. In the ultrarelativistic limit the characteristic Cherenkov angle in water is 42° for all types of charged particles.

It is, however, particularly easy to distinguish muon neutrinos from other flavours, since muons produced in charged current (CC) interactions leave long tracks in the detector. In the few GeV range under study, muons of kinetic energy E_μ typically have a track with a length of $4.25\,\mathrm{m} \cdot E_\mu/\mathrm{GeV}$ on which they emit Cherenkov radiation.[3] In contrast, high energetic electrons have on average a radiation length of 36 cm in water [24] after which they form electromagnetic cascades. The light emitted from these cascades can also be detected by the ORCA detector. How well cascades can be used to improve energy and direction reconstruction of the initial neutrino is work in progress and not scope of this work. The lifetime of the τ, produced in ν_τ CC interactions, is too short to leave tracks long enough for efficient reconstruction. However, the leptonic

[3] Other references use a muon range of $5\,\mathrm{m} \cdot E_\mu/\mathrm{GeV}$ but for the energy range considered in this work $4.25\,\mathrm{m} \cdot E_\mu/\mathrm{GeV}$ is more appropriate as can be seen from Fig. 25.

decay channels are [3]

$$\tau \to \mu + \overline{\nu}_\mu + \nu_\tau \qquad (17.41 \pm 0.04)\% \tag{13}$$

$$\tau \to e + \overline{\nu}_e + \nu_\tau \qquad (17.83 \pm 0.04)\% \tag{14}$$

and accordingly for $\overline{\tau}$. With a branching fraction of 17.8% they can thus mimic muon-type[4] events in the detector. The tau-type neutrino flux at the detector arises from flavour oscillations of muon-type and electron-type atmospheric neutrinos only. Additionally, the ν_τ CC cross section is effectively zero below 4 GeV rising to 40% of ν_μ CC cross section at 20 GeV [25]. The ν_τ background is therefore well below 10% and neglected in this work.

Hence, an efficient way for flavour tagging of the neutrino is to identify long muon tracks in the detector and conclude that the incoming neutrino was muon-type. For this reason only charged current (CC) interactions are considered, i.e. reactions of the type

$$\nu_l + N \to l^- + X \tag{15}$$

and accordingly for $\overline{\nu}_l$. The incoming (anti)neutrino ν_l of flavour $l = \{e,\ \mu,\ \tau\}$ interacts with a nucleon N in the detector medium, producing an (anti)lepton l. Whereas for high energies the charged current cross sections rise approximately linear with neutrino energy [3, chap. 40], there are deviations from σ_E/E being constant in the few GeV energy range. This region is a transition region with three contributing processes [25]:

Quasielastic scattering: Quasielastic scattering is the interactions

$$\nu_l + n \to l^- + p \qquad \overline{\nu}_l + p \to l^+ + n \tag{16}$$

where the (anti) neutrino scatters off a target neutron (proton) in a nucleus converting it into a proton (neutron). Quasielastic scattering is the dominant process for neutrino energies below 2 GeV.

Resonance production: Nucleons can be excited to form baryonic resonances, which can decay into various combinations of baryons and mesons (X in Eq. 15).

Deep inelastic scattering If the neutrino energy is high enough, the neutrino scatters off individual partons of the nucleon. X in Eq. 15 is then an hadronic shower produced in the deep inelastic scattering process.

CC cross sections for ν_μ and $\overline{\nu}_\mu$ in Fig. 6 (taken from Ref. [25]) are each approximated by two straight lines in the logarithm (base 10) of neutrino energy, $\log(E)$ (see Fig. 7). The chosen parametrisation is
for neutrinos:

$$\frac{\sigma^\nu_{CC}}{E_\nu} = \left(-0.465 \log\left(\frac{E_\nu}{\mathrm{GeV}}\right) + 0.940\right) \times 10^{-42}\,\mathrm{m^2 GeV^{-1}} \quad \text{for } 1\,\mathrm{GeV} \le E_\nu < 2.18\,\mathrm{GeV}$$

$$\frac{\sigma^\nu_{CC}}{E_\nu} = \left(-0.063 \log\left(\frac{E_\nu}{\mathrm{GeV}}\right) + 0.804\right) \times 10^{-42}\,\mathrm{m^2 GeV^{-1}} \quad \text{for } E_\nu \ge 2.18\,\mathrm{GeV}$$

[4] In the following "muon-type" refers to ν_μ and $\overline{\nu}_\mu$, accordingly for electron-type and tau-type

and for antineutrinos:

$$\frac{\sigma^{\overline{\nu}}_{CC}}{E_\nu} = \left(+0.065 \log\left(\frac{E_\nu}{\mathrm{GeV}}\right) + 0.331\right) \times 10^{-42}\,\mathrm{m}^2\ \mathrm{GeV}^{-1} \quad \text{for } 1\,\mathrm{GeV} \leq E_\nu < 2.96\,\mathrm{GeV}$$

$$\frac{\sigma^{\overline{\nu}}_{CC}}{E_\nu} = \left(-0.022 \log\left(\frac{E_\nu}{\mathrm{GeV}}\right) + 0.372\right) \times 10^{-42}\,\mathrm{m}^2\ \mathrm{GeV}^{-1} \quad \text{for } E_\nu \geq 2.96\,\mathrm{GeV}$$

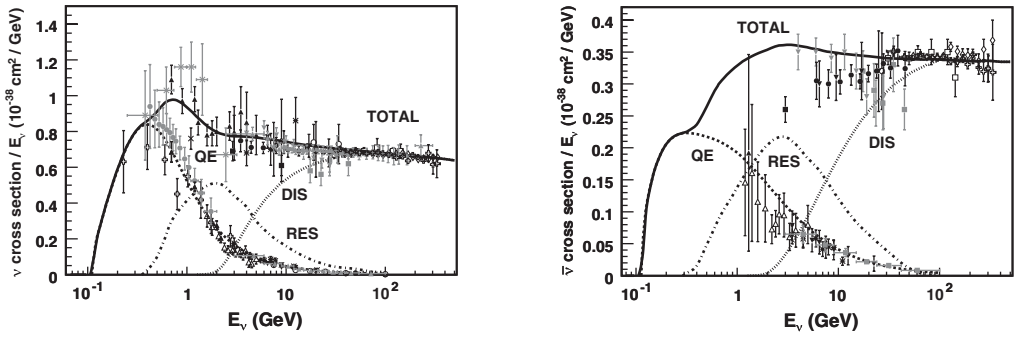

Figure 6: Total neutrino (left) antineutrino (right) per nucleon CC cross sections divided by neutrino energy. Figures taken from Ref. [25]

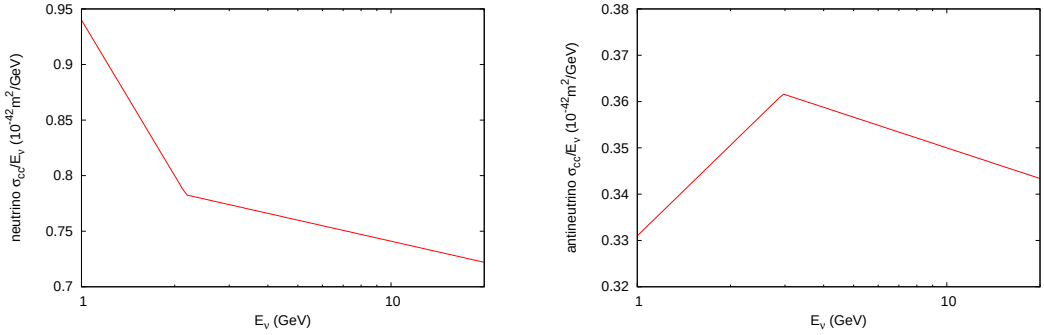

Figure 7: Chosen parametrisation of ν_μ (left) and $\overline{\nu}_\mu$ (right) CC cross sections per nucleon.

3.4. Detection

3.4.1. ORCA detector

ORCA being a first phase option for the KM3NeT detector [26] will use the digital optical modules (DOMs), each housing 31 photomultipliers (PMs), and other technology developed for KM3NeT. However, the DOMs need to be put closer together than for

astronomical observations in the TeV range – the main goal of KM3NeT – to allow efficient event reconstruction in the few GeV energy range, where the disparity of oscillation probabilities for NH and IH is large.

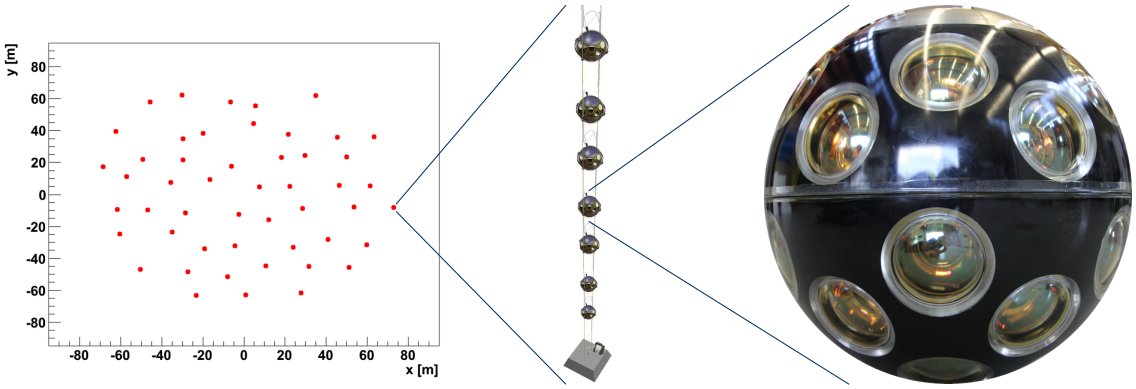

Figure 8: Footprint of the ORCA detector (left) consisting of 50 detection units (middle) with 20 DOMs each (right). Pictures taken from Ref. [26].

In current simulations the ORCA detector consists of 50 strings irregularly distributed over a circular footprint with a radius of 70 m (see Fig. 8). On each string 20 OMs are aligned with a vertical distance of 6 m. The ORCA detector therefore is a megaton-scale detector with 1.75 Mt of water inside the instrumented volume. This standard geometry is employed for the rate calculation, though it is still to be optimised for a measurement of the neutrino MH.

3.4.2. Effective volume

In this work, only signal events for which both the vertex and the whole muon track are contained within the instrumented volume are taken into account.

For a cylindrical detector with a height h of 114 m and a diameter D_d of 140 m the energy and zenith angle dependent mass of the geometric volume for neutrino interactions such that the muon track is fully contained can be expressed as [27]:

$$\begin{aligned}\rho V_{\text{geom}} &= \rho\frac{1}{2}hD_d^2 \cdot \arcsin\left(\sqrt{1-\frac{R_\mu^2}{D_d^2}\sin^2\theta_z}\right)\left(1-\frac{R_\mu}{h}\cdot|\cos\theta_z|\right) \qquad (17)\\ &= 1.12\,\text{Mt}\cdot\arcsin\left(\sqrt{1-9.22\cdot10^{-4}\frac{E_\mu^2}{\text{GeV}^2}\sin^2\theta_z}\right)\left(1-3.73\cdot10^{-2}\frac{E_\mu}{\text{GeV}}\cdot|\cos\theta_z|\right)\end{aligned}$$

assuming a muon range R_μ of $4.25\,\text{m}\cdot E_\mu/\text{GeV}$.

Detector efficiencies have been calculated at the ECAP [28] for ν_μ and $\overline{\nu}_\mu$ with simulated events using the GENHEN [29] Monte Carlo (MC) generator. The ratio of detected and all simulated muon tracks from neutrino interactions for a specific energy and zenith

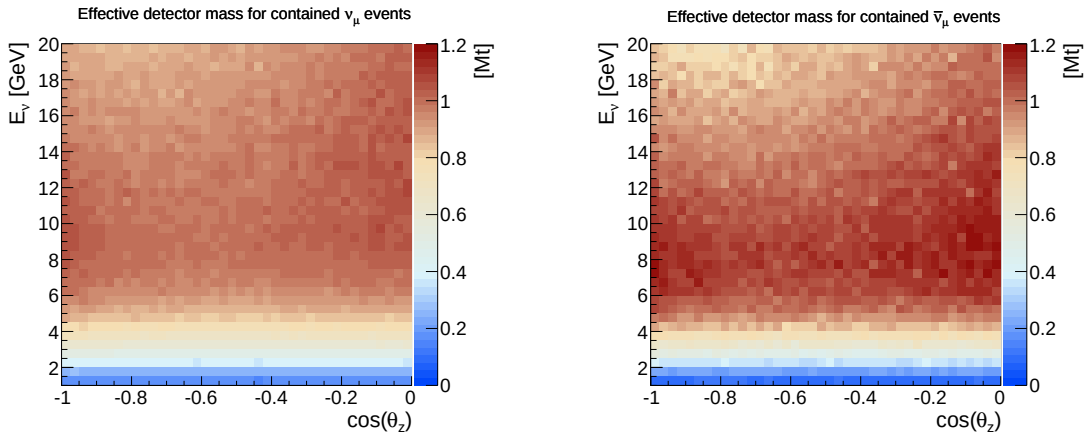

Figure 9: Effective detector mass for contained ν_μ events (left) and $\overline{\nu}_\mu$ events (right). [28]

angle was obtained requiring 10 signal hits, i.e. signals from 10 different PMTs on the light emitted by the muon.

The convolution of detector efficiencies with the geometric volume then yields the energy and zenith angle dependent effective detector mass for contained events shown in Fig. 9.

4. Rates at ORCA

4.1. Neutrino rates

In absence of neutrino oscillations, the rate density $\mathrm{d}n_\alpha(E_\nu, \cos(\theta_z^\nu))/(\mathrm{d}E_\nu\, \mathrm{d}\cos(\theta_z^\nu)\, \mathrm{d}t)$ for a specific neutrino type α is

$$\frac{\mathrm{d}n_\alpha(E_\nu, \cos(\theta_z^\nu))}{\mathrm{d}E_\nu\, \mathrm{d}\cos(\theta_z^\nu)\, \mathrm{d}t} = \frac{18 \cdot N_A}{m_{\mathrm{mol}}} \cdot 2\,\pi\, \Phi_\alpha(E_\nu, \cos(\theta_z^\nu)) \cdot \sigma_\alpha(E_\nu) \cdot \rho V_{\mathrm{eff},\alpha} \tag{18}$$

with differential neutrino flux Φ_α, CC cross section per nucleon σ_α and effective detector mass $\rho V_{\mathrm{eff},\alpha}$ as defined previously. $18 \cdot N_A/m_{\mathrm{mol}}$ is the the number of target particles per unit mass and for water the molar mass is $m_{\mathrm{mol}} = 18\,\mathrm{g/mol}$.

Including oscillation probabilities $P^{\mathrm{MH}}_{\alpha\to\beta}$, the number of neutrino events of type β per energy and zenith angle interval after time interval T is then given for hierarchy $\mathrm{MH} = \{\mathrm{NH}, \mathrm{IH}\}$ by

$$N_\beta^{\mathrm{bin,MH}} = \int \mathrm{d}E_\nu \int \mathrm{d}\cos(\theta_z^\nu) \sum_{\alpha=\mu,e} \left(P^{\mathrm{MH}}_{\alpha\to\beta}(E_\nu, \cos(\theta_z^\nu)) \cdot \frac{\mathrm{d}n_\alpha(E_\nu, \cos(\theta_z^\nu))}{\mathrm{d}E_\nu\, \mathrm{d}\cos(\theta_z^\nu)\, \mathrm{d}t} \cdot T \right) \tag{19}$$

with integral from lower to upper bin edges in E_ν and $\cos(\theta_z^\nu)$.

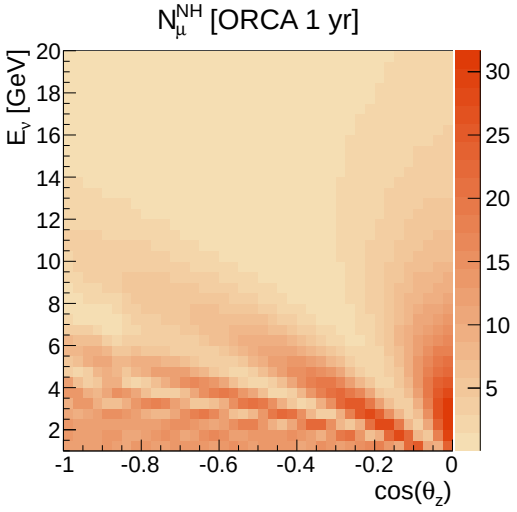

Figure 10: Number of muon-type ($\nu_\mu + \overline{\nu}_\mu$) events per year, NH assumed. The histogram for IH looks alike.

For $-1 \leq \cos(\theta_z^\nu) \leq 0$ and $1\,\text{GeV} \leq E_\nu \leq 20\,\text{GeV}$, the expected total yield per year with the ORCA detector is 4974 (4971) ν_μ events and 2109 (2095) $\overline{\nu}_\mu$ events for NH (IH). Since it will be hard to reconstruct neutrinos with energies of $\approx 1\,\text{GeV}$ the rates for $-1 \leq \cos(\theta_z^\nu) \leq 0$ and $3\,\text{GeV} \leq E_\nu \leq 20\,\text{GeV}$ are also given. These are 3316 (3316) ν_μ events and 1489 (1476) $\overline{\nu}_\mu$ events for NH (IH). The number of reconstructed events thus decreases significantly when setting a lower limit on the neutrino energy, E_ν.

The expected differential rate for neutrinos with $1\,\text{GeV} \leq E_\nu \leq 20\,\text{GeV}$ was obtained using the necessary ingredients discussed in Sec. 3. The resulting rates for NH and IH (shown for NH in Fig. 10) do not show a difference that is visible to the naked eye. A closer look on the asymmetry between the two hierarchies is therefore necessary.

4.2. Asymmetry

The statistical asymmetry of muon-type events between NH and IH can be defined for each bin as [8]

$$\mathcal{A}_i^\mu = \frac{N_{\mu,i}^{\text{IH}} - N_{\mu,i}^{\text{NH}}}{\sqrt{N_{\mu,i}^{\text{NH}}}} \tag{20}$$

where $N_{\mu,i}^{\text{NH}}$ ($N_{\mu,i}^{\text{IH}}$) is the number of muon-type events for NH (IH) in the respective bin i. The resulting asymmetry is depicted in Fig. 11.

The choice of asymmetry in Eq. 20 is such that it corresponds to a statistical significance. Given that the significances of individual bins are independent of each other, the cumulative significance $\mathcal{S}$ can be calculated from the significances $\mathcal{A}_i$ of individual bins

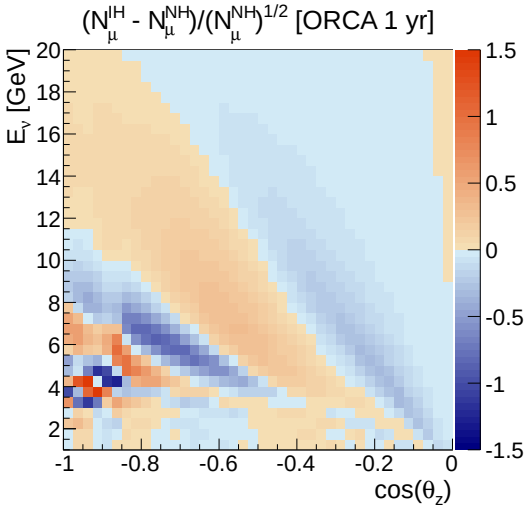

Figure 11: Statistical asymmetry between NH and IH for ORCA after 1 year of exposure

as follows [8]:

$$\mathcal{S} = \sqrt{\sum_{\text{bins } i} \mathcal{A}_i{}^2}, \tag{21}$$

which for the muon-type neutrino asymmetry in Fig. 11, i.e. for one year in the ORCA detector, is $\mathcal{S} = 7.8\,\sigma$.

This raises hope, that the neutrino mass hierarchy can be determined with the ORCA detector. However, besides systematic uncertainties of the neutrino oscillation parameters, the fluxes and the CC cross sections, neither detector efficiencies nor background have been taken into account in this calculation. Furthermore, as already stated above, neutrinos cannot be measured directly. Thus the effect will be smeared out when the neutrino direction and energy is reconstructed from the muons and the hadronic shower produced in CC interactions.

5. Kinematic smearing

The flavour of neutrinos can only be tagged if the flavour of the charged lepton produced in CC interactions is identified. As stated above, flavour tagging works best for muon neutrinos, since muons leave long tracks as a unique signature in the detector. By contrast, an electron track is much shorter, and for this work it is therefore assumed that electron neutrinos can be distinguished from muon neutrinos with the ORCA detector with an efficiency of 100%. Once results on the efficiency of flavour tagging are available, the rate for mis-tagged electron neutrinos may be included in the calculations performed in this work.

In the low energy range under study the direction of the produced muon deviates significantly from the direction of the incoming neutrino. So even presuming perfect detector resolution, the E_ν–$\cos\theta_z$ distribution of muon-type neutrinos in Fig. 10 is smeared by the kinematics of CC interactions.

5.1. Gaussian smearing in energy and zenith angle

To compare results obtained with the calculation for ORCA above to Ref. [8], the neutrino rates from Sec. 4.1 are smeared independently in the space angle γ between neutrino and produced muon and in neutrino energy E_ν with a Gaussian distribution

$$G\left(\boldsymbol{x}, x_0, \sigma_x\right) = \frac{1}{\mathcal{N}} \exp\left(-\frac{(\boldsymbol{x} - x_0)^2}{2\sigma_x^2}\right), \quad \boldsymbol{x} = E_\nu, \gamma \tag{22}$$

with x_0 being the mean and σ_x being the width of the Gaussian.

For Gaussian smearing in energy E_ν, the centre of the bin to be smeared is set as the mean $E_{\nu,0}$. The distribution is then integrated from the lower to the upper bin edges.[5] The angular part however cannot just be smeared with a Gaussian in zenith angle θ_z, but has to be treated in spherical coordinates.

First, following Ref. [8], a Gaussian distribution $G(\boldsymbol{\gamma}, \gamma_0, \sigma_\gamma)$ is assumed. The width of the Gaussian is taken to be the RMS value of the scattering angle [30] between neutrino and muon: $\sigma_\gamma = \gamma_{\mathrm{RMS}} = \sqrt{\frac{m_p}{E_\nu}}$, where m_p denotes the nucleon mass.

For σ_γ sufficiently small (i.e. $\sigma_\gamma \ll 2\pi$), the angle γ between two directional vectors can be expressed in terms of spherical coordinates $\theta_z \in [0:\pi]$ and $\varphi \in [0:2\pi]$ as [31]

$$\gamma = \mathrm{acos}\left(\sin(\theta_{z,1})\sin(\theta_{z,0})\cos(\varphi_1 - \varphi_0) + \cos(\theta_{z,1})\cos(\theta_{z,0})\right) \tag{23}$$

Without loss of generality φ_0 can be set to zero, since for the mass hierarchy only θ_z is relevant and φ is integrated from 0 to 2π. $\mathcal{N}$ is the integral of the exponential in Eq. 22 with arbitrary but fixed $\theta_{z,0} \in [0:\pi]$ over the whole sphere with surface element $\mathrm{d}\Omega = \sin(\theta_z)\mathrm{d}\theta_z\mathrm{d}\varphi$

$$\mathcal{N} = \int_0^{2\pi}\int_0^{\pi} \exp\left(-\frac{\left(\mathrm{acos}\left(\sin(\theta_{z,1})\sin(\theta_{z,0})\cos(\varphi_1) + \cos(\theta_{z,1})\cos(\theta_{z,0})\right)\right)^2}{2\sigma_\gamma^2}\right)\sin(\theta_z)\mathrm{d}\theta_z\mathrm{d}\varphi \tag{24}$$

For binwise smearing, θ_0 is set to the central value of the bin that is smeared. The integral for the angular part is then calculated for each bin from the lower to the upper bin edges in θ_1 and from 0 to 2π in φ_1.

Alltogether the number of events in bin (i, j) ($\cos(\theta_z^\nu)$ bin i, energy bin j) after smearing the events from bin (k, l) is

[5] This method provides correct results unless the bin widths are large compared to the width of the Gaussian.

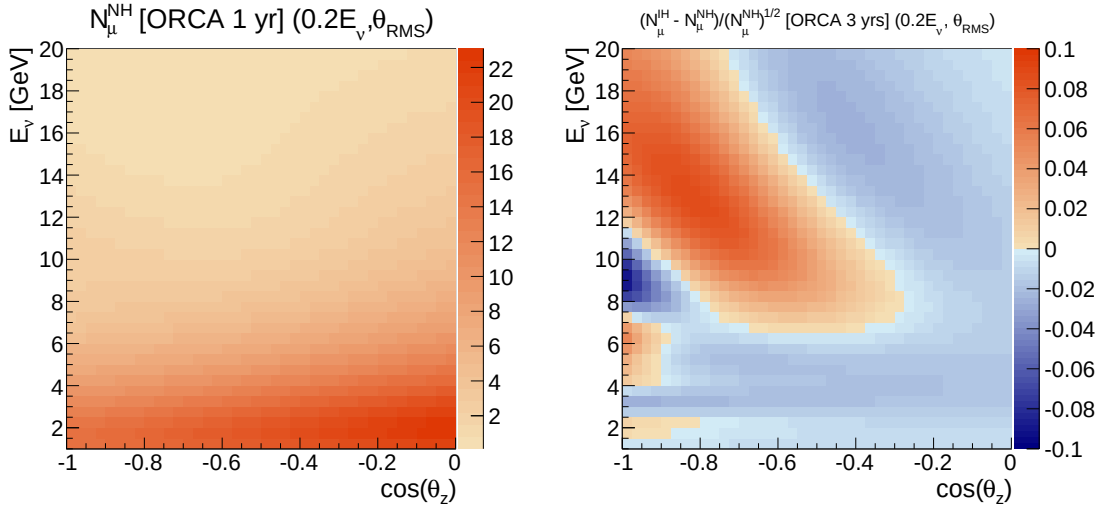

Figure 12: NH rate and hierarchy asymmetry for Gaussian smearing in both angle and neutrino energy ($\sigma_E = 0.2 \cdot E_\nu$, $\sigma_\gamma = \theta_{RMS}$).

$$N_{ij}^{\mathrm{sm}(kl)} = \frac{1}{\sqrt{2\pi}\sigma_{E_{l,0}} \cdot \mathcal{N}_k} \int_{E_j(low)}^{E_j(up)} \mathrm{d}E \int_{\theta_z^i(low)}^{\theta_z^i(up)} \mathrm{d}\theta_1 \int_0^{2\pi} \mathrm{d}\varphi_1 \; G\left(\boldsymbol{E}, E_{l,0}, \sigma_{E_l}\right) \cdot G\left(\boldsymbol{\gamma}, \gamma_{k,0}, \sigma_{\gamma_k}\right) \cdot \sin\theta_1 \tag{25}$$

where γ is substituted as defined in Eq. 23. This smearing is done for all bins (k, l) yielding the histograms in Fig. 12. This is conform to the asymmetry in Ref. [8], taken into account the smaller effective volume for the ORCA calculation.

5.2. Simulated data motivated smearing

Simulated data [29] has been used to test if the distribution of the scattering angle between the incoming neutrino and the produced muon can be approximated by a simple Gaussian distribution. The distribution of the space angle between neutrino and muon direction is depicted for ν_μ with $8.0 < E_\nu < 8.5\,\mathrm{GeV}$ in Fig. 13. A Gaussian distribution $G(\boldsymbol{\gamma}, \gamma_0, \sigma_\gamma)$ around the direction of the incoming neutrino transfers to a distribution $2\pi \sin\gamma \times G(\boldsymbol{\gamma}, \gamma_0, \sigma_\gamma)$ when looking only at the absolute value of the space angle. From Fig. 13 follows that a Gaussian distribution with $\sigma_\theta = \theta_{\mathrm{RMS}}$ does not describe the space angle distribution between the muon and ν_μ . Also, a Gaussian with smaller σ_γ does not match the true distribution of the space angle, because for large scattering angles the Gaussian distribution then falls of too quickly and underestimates the amount of muons with large γ. Additionally, the space angle distribution (here depicted for ν_μ only) is contracted towards smaller scattering angles for $\overline{\nu}_\mu$. This is because the antineutrino tends to deposit less of its energy into the hadronic shower than the neutrino. This feature is commonly expressed in terms of the Bjorken y, also referred to as inelasticity

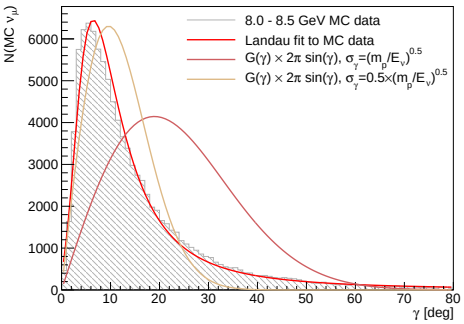

Figure 13: Space angle distribution for ν_μ from simulated data [29]. N(MC ν_μ) is the number of Monte Carlo events for ν_μ .

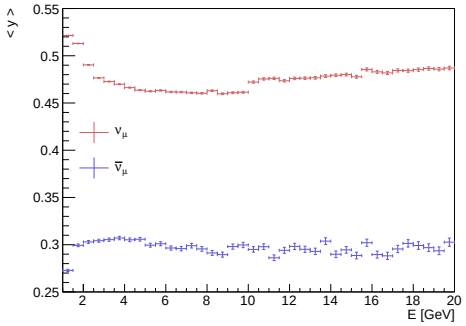

Figure 14: Mean Bjorken $\langle y \rangle$ for ν_μ and $\overline{\nu}_\mu$ of the MC sample

parameter

$$y = 1 - \frac{E_\mu}{E_\nu}. \tag{26}$$

The mean Bjorken y of the MC sample used is $\langle y \rangle_\nu^{\mathrm{MC}} = 0.49$ for neutrinos and $\langle y \rangle_{\overline{\nu}}^{\mathrm{MC}} = 0.30$ for antineutrinos as can be seen from Fig. 14, which is in reasonable agreement with the values $\langle y \rangle_\nu^{\mathrm{lit}} = 0.483$ for neutrinos and $\langle y \rangle_{\overline{\nu}}^{\mathrm{lit}} = 0.333$ for antineutrinos at 10 GeV given in [32, Tab. 1,2]. Below 5 GeV the contributions of resonance production and quasi-elastic scattering have a strong influence on the actual distribution of the Bjorken y, but the y distribution is steady in the energy region above (see Appendix C).

A parametrisation of the total differential cross section for CC neutrino nucleon scattering is not at hand, so in the scope of this work a distribution function had to be found that approximates the space angle distribution of muon-type neutrinos sufficiently well.

An empirical observation is that for a more accurate smearing, corresponding to the transition from neutrino direction to muon direction, the space angle distribution of MC data for ν_μ and $\overline{\nu}_\mu$ can be fit with a Landau distribution $\mathrm{Landau}(\boldsymbol{x}, \mathrm{MPV}, w)$, with MPV the most probable value and w a constant corresponding to the width of the distribution. Fitting MC data of a specific energy with a Landau distribution yields values for the energy dependent constants MPV and w (see Fig. 15). In the MC sample examined MPV and w are linearly interconnected (see left side of Fig. 15)

$$w_\nu = 0.36 \cdot \mathrm{MPV}_\nu + 0.38 \tag{27}$$

$$w_{\overline{\nu}} = 0.30 \cdot \mathrm{MPV}_{\overline{\nu}} + 0.19 \tag{28}$$

Additionally w can be set into relation with the neutrino energy E_ν as follows (see right side of Fig. 15):

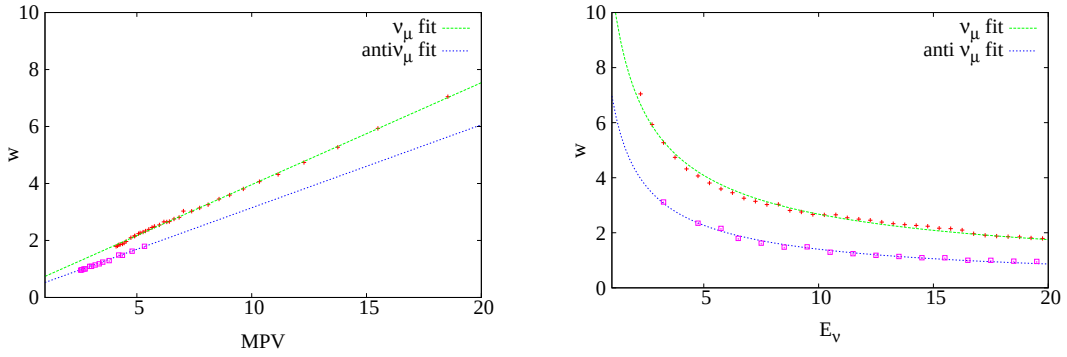

Figure 15: Fits to express MPV and w in terms of neutrino energy E_ν leading to a Landau distribution dependent on $E_{\nu,0}$ and space angle γ between neutrino and muon only. Left: w in terms of the MPV. Right: w in terms of the neutrino energy E_ν.

$$w_\nu = 11.4 \cdot \left(\frac{m_p}{E_\nu}\right)^{0.61} \tag{29}$$

$$w_{\overline{\nu}} = 7.28 \cdot \left(\frac{m_p}{E_\nu}\right)^{0.70} . \tag{30}$$

Thus, taking these values for ν_μ and $\overline{\nu}_\mu$, the obtained Landau distribution is a function depending on neutrino energy and space angle γ only. Smearing the E_ν–$\cos(\theta_z^\nu)$ distribution in θ_z^ν separately for ν_μ and $\overline{\nu}_\mu$ is done similarly to the above smearing of the angular part, but with $G(\boldsymbol{\gamma}, \gamma_0, \sigma_\gamma)$ replaced by $\textsc{Landau}(\boldsymbol{\gamma}, \gamma_0, E_0)/(2\pi \cdot \sin\gamma)$.

Just as above, γ is a substitute for the space angle defined in Eq. 23. Again, each bin is smeared by setting the bin center to be the $\theta_{z,0}$ and $E_{\nu,0}$ of the probability distribution function and integrating for all bins.

This MC motivated Landau smearing, "MCγ", yields the $E_\nu - \cos\theta_z^\mu$ distribution for perfect detector resolution depicted in Fig. 16.

Then, in a second step, detector resolution can be taken into account. In Fig. 17 an energy resolution of $\sigma_E = 0.1E_\nu + 1\,\text{GeV}$ on muon and shower energy and an angular resolution of $\sigma_\gamma = 5°$ on the muon were assumed. Again, the effect is washed out significantly, but not as much as in the case of Gaussian smearing with the RMS value of the scattering angle in Fig. 12.

Applying these two subsequent steps corresponds to a reconstruction strategy, in which the direction of the incoming neutrino is reconstructed from the muon direction only. Contrarily, the neutrino energy is reconstructed from the sum of shower energy and muon energy.

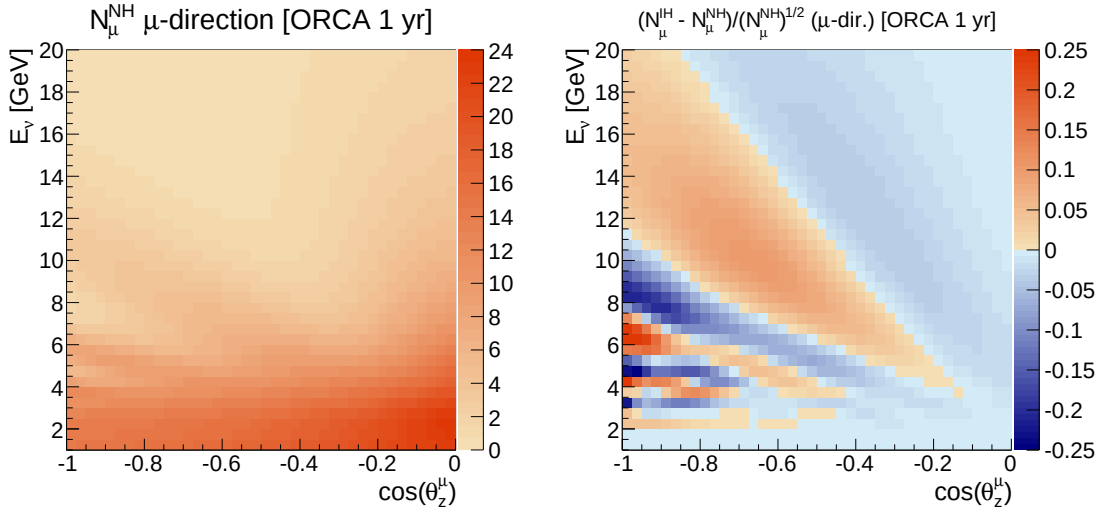

Figure 16: NH rates (left) and asymmetry between NH and IH (right) after smearing in θ_z^ν according to a Landau distribution fit to MC data (MCγ).

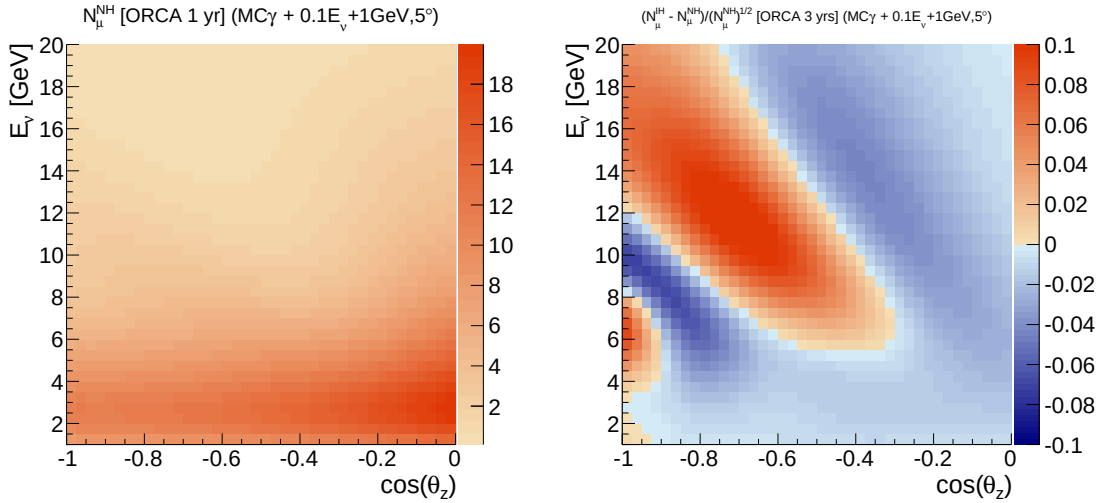

Figure 17: NH rates (left) and asymmetry between NH and IH (right) after MCγ smearing and subsequent smearing with $\sigma_\gamma = 5°$ and $\sigma_E = 0.1 \cdot E_\nu + 1\,\text{GeV}$ to account for detector resolution. The asymmetry is depicted for 3 years of ORCA.

The uncertainty of the true neutrino direction can possibly be further reduced by reconstructing the shower.

6. Log-likelihood ratio statistic and discrimination power

To distinguish between NH and IH, a statistical test is needed that can be applied to a measured distribution of atmospheric neutrino events.[6]

6.1. Log-likelihood ratio

The number of events k measured in a bin i will be Poisson distributed around a mean μ_i^{MH}, which is the expected number of events in this bin for either NH or IH. The likelihoods, that a measured number of events in a bin is conform to the expected number of events in this bin assuming NH and IH can be calculated as

$$L_i^{\mathrm{MH}}(k_i|\mu_i^{\mathrm{MH}}) = \frac{(\mu_i^{\mathrm{MH}})^{k_i}\exp(-\mu_i^{\mathrm{MH}})}{k_i!}, \quad \mathrm{MH} = \mathrm{NH},\,\mathrm{IH}. \tag{31}$$

The likelihood that the measured distribution in all bins of the $E_\nu - \cos\theta_z$ histogram fits the expected distribution is then

$$L(\mathrm{data}|\mathrm{MH}) = \prod_i L_i^{\mathrm{MH}}(k_i|\mu_i^{\mathrm{MH}}). \tag{32}$$

The dominance of one likelihood over the other can be expressed as a likelihood ratio

$$R(\mathrm{data}) = \frac{L(\mathrm{data}|\mathrm{NH})}{L(\mathrm{data}|\mathrm{IH})}. \tag{33}$$

However, it is more convenient to take the natural logarithms of likelihoods and likelihood ratio and calculate log-likelihoods

$$\lambda(\mathrm{data}|\mathrm{MH}) = \log(L(\mathrm{data}|\mathrm{MH})) = \sum_i \log(L_i^{\mathrm{MH}}(k_i|\mu_i^{\mathrm{MH}})) \tag{34}$$

and the log-likelihood ratio

$$\rho(\mathrm{data}) = \frac{\lambda(\mathrm{data}|\mathrm{NH})}{\lambda(\mathrm{data}|\mathrm{IH})} = \sum_i \left(k_i \cdot \log\mu_i^{\mathrm{NH}} - k_i \cdot \log\mu_i^{\mathrm{IH}} + \mu_i^{\mathrm{NH}} - \mu_i^{\mathrm{IH}}\right) \tag{35}$$

instead.

[6] The notation in the equations for the calculation of log-likelihood ratios follows Ref. [33]. It was proven in Ref. [34] that for testing two simple hypotheses, a test like the one that will be used in this work has indeed the highest discrimination power. "Simple" in this context means that for NH and IH the probability distribution functions, or equivalently the E_ν and θ_z^ν dependent rates of neutrino events for NH and IH, are precisely known. For a mass hierarchy measurement this is true up to uncertainties of the different parameters used for the calculation.

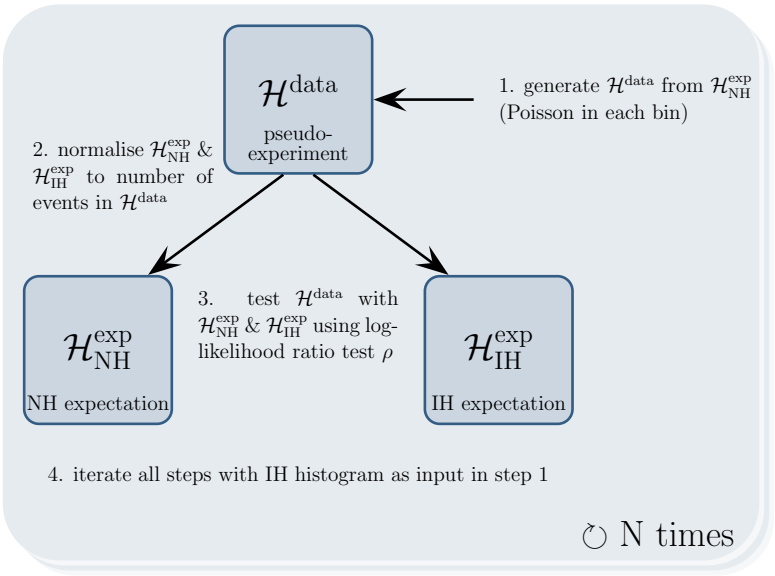

Figure 18: Chart illustrating how the log-likelihood ratio ρ(data) distribution is obtained

In a real measurement, ρ(data) will be calculated taking the measured distribution and comparing it to the NH and IH expectation rates. To be able to draw a conclusion from a measured ρ(data), probability densities to obtain a certain value for ρ(data) for one true hierarchy, i.e. NH or IH, are needed. To this end, pseudo-experiments are generated as follows (for illustration, see Fig. 18):

1. First, NH is assumed to be the true hierarchy. To simulate an experiment, the NH expectation histogram ($\mathcal{H}^{\text{exp.}}_{\text{NH}}$) is normalised to the duration of measurement, T. For the pseudo-experiment, the number of neutrinos detected in a bin will be given by a random number generated from a Poisson distribution with expectation value taken from the renormalised NH expectation histogram. A "pseudo-measured" histogram ($\mathcal{H}^{\text{data}}$) filled with Poisson random numbers according to $\mathcal{H}^{\text{exp.}}_{\text{NH}}$ is generated.

2. Then the histograms of expected events for NH and IH are normalised to the "pseudo-measured" number of events. This prevents offsets for one hierarchy because of the small differences in the expected rates for NH and IH. In a real experiment this may also compensate for uncertainties of the overall flux normalisation.

3. Now the log-likelihood ratio ρ(data), as defined in Eq. 35, is calculated for the pseudo-experiment taking the values from the renormalised NH (IH) expectation histogram as μ_i^{NH} (μ_i^{IH}). This yields a ρ(data) value with NH being the true hierarchy.

4. Finally the same is done assuming IH to be the true hierarchy. The result is a ρ(data) value for IH as the true hierarchy.

After many pseudo-experiments the ρ(data) values are Gaussian distributed around a positive mean $\rho_{0,\mathrm{NH}}$ for NH as the true hierarchy. The distribution of log-likelihood ratios ρ(data) with an IH input is Gaussian around a negative mean $\rho_{0,\mathrm{IH}}$. Longer measuring times T will lead to a higher ability to distinguish between NH and IH. For small T the log-likelihood ratio distributions overlap significantly. For longer measuring times T the two Gaussians for NH and IH increasingly seperate from each other as can be seen in Fig. 19 for a log-likelihood ratio test with the unsmeared E_ν–$\cos(\theta_z^\nu)$ distribution.

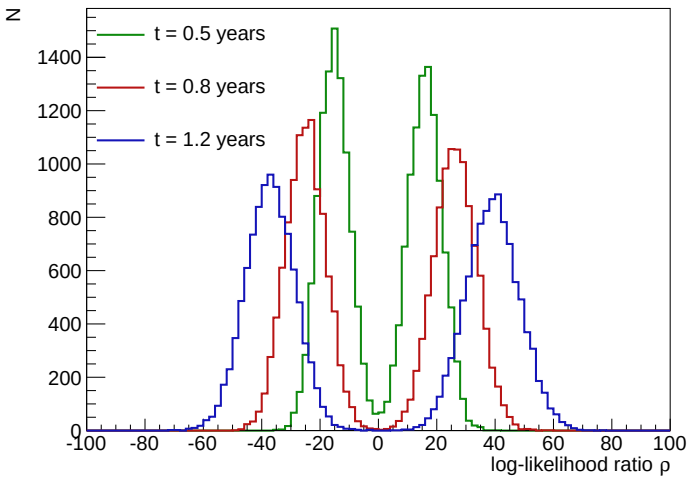

Figure 19: Log-likelihood ratio ρ distibutions for NH and IH for different measuring times t

6.2. P-value

For a discovery, one of the two hierarchies has to be excluded with at least $5\,\sigma$ statistical significance. Therefore, the p-value is chosen to be the probability of being able to exclude one of the two hierarchies with $5\,\sigma$.

The two resulting distributions for the log-likelihood ratio values are fit with a Gaussian distribution each ($G(\sigma_{\mathrm{NH}}, \rho_{0,\mathrm{NH}})$, $G(\sigma_{\mathrm{IH}}, \rho_{0,\mathrm{IH}})$). If uncertainties of the model parameters are neglected, IH will be excluded if ρ(data) calculated from experimental data falls outside the $\rho_{0,\mathrm{IH}} \pm 5\sigma_{\rho_{\mathrm{IH}}}$ region, and accordingly for NH. The widths ($\sigma_{\rho_{\mathrm{IH}}}$ and $\sigma_{\rho_{\mathrm{NH}}}$) are obtained from a Gaussian fit to the distribution. This is depicted in Fig. 20.

In the central region that is less than $5\sigma_{\mathrm{NH}}$ from the Gaussian mean $\rho_{0,\mathrm{NH}}$ and less than $5\sigma_{\mathrm{IH}}$ from the Gaussian mean $\rho_{0,\mathrm{IH}}$, none of the two hierarchies can be excluded with a certainty of 5σ. The p-value is therefore the ratio of all events that fall outside this region. If the log-likelihood ratio of measured data ρ(data) lies in the positive

(negative) allowed region, IH (NH) will be excluded. The shaded regions on the left and on the right in Fig. 20 are more than 5σ from both expectations. If a real measurement resulted in a ρ(data) value in one of these regions, this result would be unphysical [19] and therefore most probably due to wrong assumptions in the calculation of the expected rate distibution.

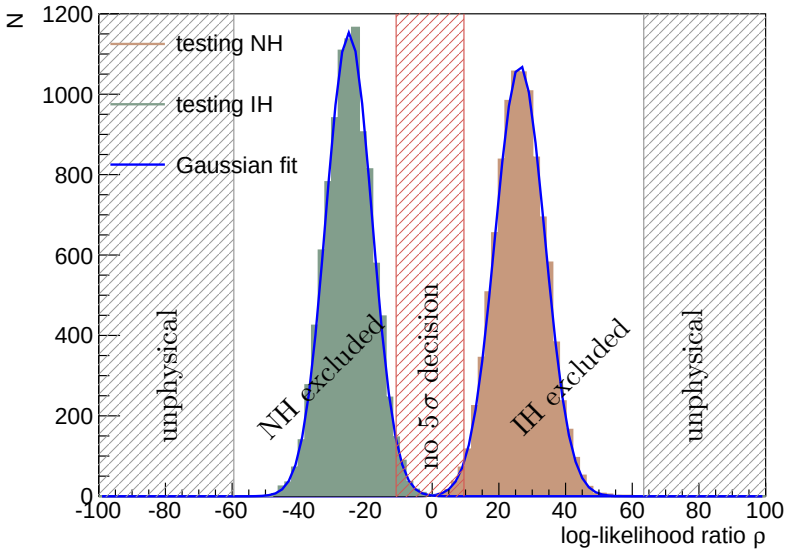

Figure 20: Log-likelihood ratio distribution after 10,000 pseudo-experiments for NH and IH as true hierarchy. In the central shaded region, no 5σ distinction between the two hierarchies is possible. Log-likelihood ratio values in the outer shaded regions are unphysical.

7. Estimate for ORCA exposure needed for MH determination

The p-value, defined above as the probability of being able to exclude one hierarchy with $5\,\sigma$, can be calculated for different durations of measurement T. For long T the two hierarchies are more distinguishable and hence the p-value approaches 1. Figure 21 shows the evolution of the p-value with increasing measuring time T for contained neutrino events calculated as set out in Sec. 4.1. The p-value approaches 1 already within one year given perfect resolution on the neutrino. Mind, that for this calculation none of the uncertainties of the various input parameters for the rate calculation are included.

From Fig. 21 it can be concluded, that it is necessary to be able to reconstruct neutrinos with energies above 3 GeV. The fact that the energy region below 3 GeV does not have a sizeable effect on the amount of exposure needed for MH determination can also

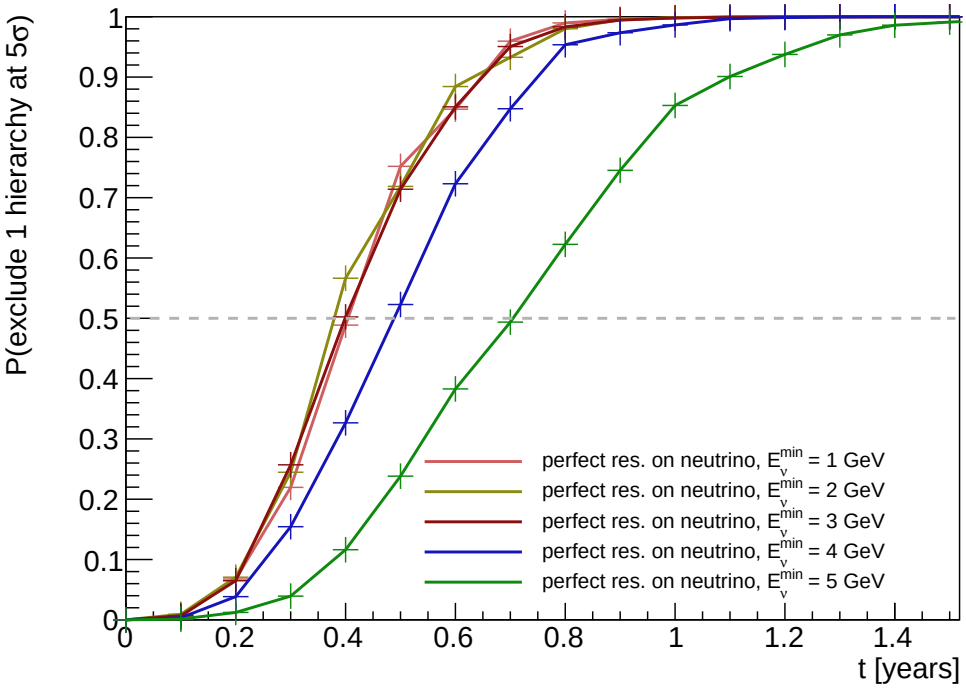

Figure 21: P-value evolution calculated for threshold energies from 1–5 GeV given perfect energy and angular resolution on the neutrino

be seen in the statistical asymmetries (smeared and unsmeared) shown above[7]. Below 3 GeV the asymmetry between NH and IH is ≈ 0. For threshold energies beyond 3 GeV the time needed for a probability of more than 50% to have a $5\,\sigma$ distinction increases rapidly, in the unsmeared case from 0.4 to 0.5 years for a threshold energy of 4 GeV. Almost twice the time is needed (0.4 years $\leftrightarrow$ 0.75 years in Fig. 21) in the unsmeared case already for a threshold energy as low as 5 GeV.

Taking into account the kinematic angle between muon and neutrino, the timescale to reach a p-value of more than 50% will increase significantly even with a perfect reconstruction of the muon direction (Fig. 22, green dots).

For the simple approximation of a Gaussian distribution on the angular reconstruction with the RMS value of the scattering angle as the width and an energy resolution of 20%, the duration to reach a p-value of 0.5 is 50 years for contained events in a 50 string ORCA detector (See Appendix D).

The absolute timescale for a MH determination with ORCA, will ultimately depend on the possibility to reconstruct the energy and direction of the neutrino from energy and direction of the produced muon and hadronic shower. To get a feeling for the effect of detector resolution, time dependent p-values are given for a space angle resolution $\sigma_\gamma = 5^\circ$ on the muon and for energy resolutions

$$\sigma_{E_\nu} = 1\,\mathrm{GeV} + \varepsilon \cdot E_\nu \tag{36}$$

on the distribution after MC based kinematic smearing, MCγ. This choice of σ_{E_ν} is quite arbitrary since the uncertainties of energy reconstruction and even the strategy for event reconstruction to measure the MH is unclear up to now. However, there will always be a constant term for all neutrino energies due to the uncertainties of the reconstruction of the muon start and end points. Additionally, the uncertainties of the shower and muon energy rise proportional to the neutrino energy [27], which motivates the second term.

The exposure dependent p-values for $\varepsilon = \{5\%, 10\%, 15\%, 20\%\}$ are presented in Fig. 22. None of the values for ε yields short measuring times for a successfull MH measurement with the assumed ORCA effective volume. As a conclusion, the energy reconstruction has to be better than assumed in Eq. 36. With MCγ smearing in angle alone a p-value of 0.5 is reached in less than 10 years. Energy resolution thus has a severe effect on the MH determination with ORCA.

The p-values calculated are further reduced by various effects: (a) Flavour tagging efficiencies will be certainly less than the assumed 100% in the low energy region. Also, (b) uncertainties of the various input parameters (eg. oscillation parameters, flux of atmospheric neutrinos, CC cross sections, ...) have not yet been accounted for nor (c) the decrease in sensitivity to a MH determination after quality cuts on the detected events.[8] Contrarily, including electron- and tau-type neutrino rates may have a positive effect on a MH determination with ORCA. Also reconstruction of the hadronic shower to determine the neutrino direction has not yet been considered in this calculation.

[7] See Fig. 11, Fig. 12, Fig. 16 and Fig. 17

[8] Notice that due to the different kinematics of the interaction, quality cuts will preferentially reject ν_μ events thus increasing the amount of $\overline{\nu}_\mu$ events. This decreases the statistical asymmetry, which arises mainly from the lower flux and cross section of $\overline{\nu}_\mu$ compared to ν_μ.

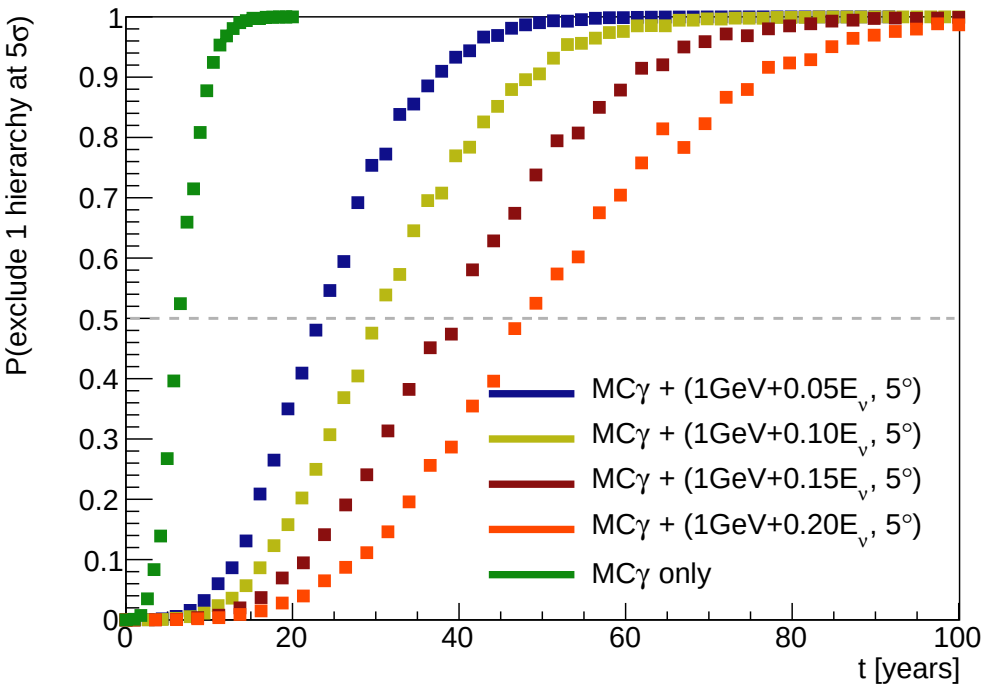

Figure 22: Time evolution of p-values for different assumptions on energy resolution.

8. Uncertainties of the neutrino oscillation parameters

Neutrino oscillation parameters are only known within some errors (cf. 1σ ranges in Tab. 1 and [23] for 3σ ranges) and the CP violating phase δ_{CP} has not been measured yet. Hence, the effects of uncertainties of the different oscillation parameters on the MH determination using log-likelihood ratio statistics have to be studied. To this end, rate histograms calculated for the central value $\pm 3\sigma$ and $\pm 1\sigma$ for each parameter[9] are compared to the expectation histograms for NH and IH. Throughout this section, the rate histograms after MCγ smearing are taken to stay independent of a specific detector resolution. The log-likelihood ratios ρ(data) are calculated for $T = 15$ years of mesuring time, where the p-value for the central value case has reached 1. However, just calculating p-values when testing a $\pm 1\,\sigma$ or $\pm 3\,\sigma$ distribution is insufficient, since the Gaussian distributed log-likelihood ratios may be translated to higher or lower values. This effect is very serious for Δm^2, as can be seen for $\Delta m^2 \pm 1\,\sigma$ from Fig. 24. Here, the log-likelihood ratios obtained from testing a $\Delta m^2 - 1\,\sigma$ input are positive for both hierarchies. For $\Delta m^2 + 1\,\sigma$ all ρ(data) values are negative. If $\Delta m^2 + 1\,\sigma$ is the true value for the large mass difference, a measurement with measuring time $T = 15$ years will exclude NH by mistake if NH is realised in nature and the central value is assumed for Δm^2. In most cases, however, the measured log-likelihood ratio will be unphysical.

The reason for the translation of the log-likelihood ratios is that positive and negative asymmetry regions shift if certain oscillation parameter values differ from the central value. This effect is most obvious for $\Delta m^2 \pm 3\,\sigma$ given in Fig. 23. Here, especially for straight upgoing events ($\cos\theta_z = -1$) negative asymmetry regions are converted into positive asymmetry regions when varying Δm^2 in the $\pm 3\sigma$ range around the central value.

For uncertainties of the different oscillation parameters, p-values are calculated taking the limits for the five different regions – the NH acceptance region, the IH acceptance region, the central "no decision" region, and the two unphysical regions – from the log-likelihood ratio calculation for the central value. Besides the p-value, the probability to successfully determine the neutrino mass hierarchy realised in nature, there are two more important quantities:

- The fraction of log-likelihood ratio values ρ(data) in the unphysical region, and
- the fraction of ρ(data) leading to wrong decision on the mass hierarchy.

The first item indicates that assumptions in the rate calculation are unnatural and have to be refined, while the second item is more serious because the measurement would exclude the true hierarchy by mistake. The probabilites to get an unphysical result and to make a wrong MH determination for variations in the oscillation parameters' values are presented in Tab. 2. Table 3 contains the p-values to get a correct decision for one of the two hierarchies. The values for ρ(data) only have wrong sign for one of the two hierarchies when varying the large mass difference, Δm^2. Uncertainties of the

[9] For the CP phase, only values for $\pm 1\sigma$ exist.

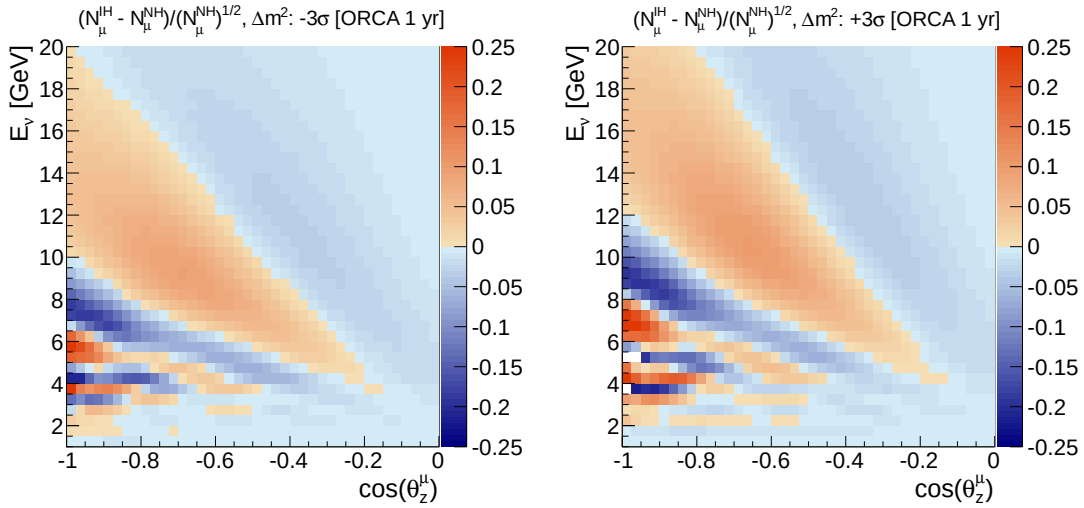

Figure 23: Asymmetry for $\Delta m^2 - 3\sigma$ and $\Delta m^2 + 3\sigma$ is shifted with respect to the central value case (see Fig. 16).

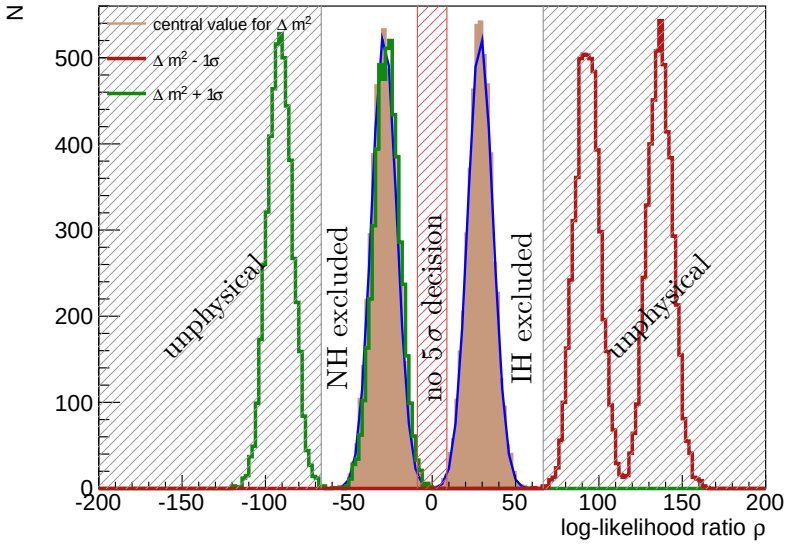

Figure 24: The log-likelihood ratio ρ can be formed testing a $\Delta m^2 \pm 1\,\sigma$ input with the central value expectations. The log-likelihood ratio distributions for NH and IH are both shiftet to positive values for $\Delta m^2 - 1\,\sigma$ and to negative values for $\Delta m^2 + 1\,\sigma$.

Table 2: Probabilities to make a wrong decision on MH and probabilities to get unphysical results for different variations of the oscillation parameters

false pos. [%]	-3σ	-1σ	$+1\sigma$	$+3\sigma$	unphys. [%]	-3σ	-1σ	$+1\sigma$	$+3\sigma$
θ_{12}	0.0	0.0	0.0	0.0	θ_{12}	0.0	0.0	0.0	0.0
θ_{13}	5.1	0.0	0.0	0.2	θ_{13}	0.3	0.0	0.0	3.0
θ_{23}	0.0	0.0	0.0	0.0	θ_{23}	0.0	0.0	0.0	0.0
δm^2	0.0	0.0	0.0	0.0	δm^2	0.0	0.0	0.0	0.0
Δm^2	0.0	0.0	49.6	0.0	Δm^2	100.0	100.0	50.0	100.0
δ_{CP}	–	0.0	0.0	–	δ_{CP}	–	0.0	0.0	–

Table 3: P-value for correct MH discrimination with oscillation parameters varied in the $\pm 3\sigma$ range

p-value	-3σ	-1σ	$+1\sigma$	$+3\sigma$
θ_{12}	1.00	1.00	0.99	0.98
θ_{13}	0.57	0.96	0.98	0.78
θ_{23}	0.96	0.99	1.00	0.98
δm^2	0.98	0.99	1.00	1.00
Δm^2	0.00	0.00	0.00	0.00
δ_{CP}	–	1.00	0.99	–

CP violating phase δ_{CP}, the small mass difference δm^2 and the mixing angles θ_{12} and θ_{23} have negligible effect on MH determination. Uncertainties of θ_{13}, although possibly decreasing the p-value significantly, give at most a 5% chance for a decision in favour of the wrong hierarchy. Also, the amount of unphysical results is small ($< 3\%$).

Varying the large mass difference Δm^2 however has a dramatic effect on the mass hierarchy determination using a binned log-likelihood ratio as in this work.

Two possibilities to overcome this problem are: (a) to find a way to limit down uncertainties of Δm^2, either with ORCA or other experiments or (b) to exclude regions where there negative asymmetry regions quickly shift into positive asymmetry regions, namely the region of straight upgoing tracks. The second possibility however, leads to a severe decrease in sensitivity and thus increases the exposure needed for high p-values for successful MH discrimination.

9. Conclusion and outlook

In this thesis it was shown that the timescale for a successful neutrino MH measurement with ORCA using a binned log-likelihood ratio test rapidly rises with increasing the uncertainties of the neutrino direction and energy reconstruction. For the effective volume chosen in this work, the MH asymmetry is small below 3 GeV. However, a neu-

trino energy threshold above 3 GeV will rapidly force up the measuring times needed for high probability to determine the neutrino MH. The effect of the uncertainty of the neutrino oscillation parameters on the binned log-likelihood ratio test used in this thesis was presented. Uncertainties of the large mass difference Δm^2 state a problem. The uncertainty of θ_{13} also affects MH determination significantly, whereas the effects of the other neutrino parameters are negligible. However, the robustness of this binned log-likelihood ratio estimate has not yet been checked for the uncertainties of the other input parameters, which are largest for the neutrino flux and the cross section at low energies. Moreover the rate of mis-reconstructed atmospheric muons and the effect of the other neutrino flavours has not been included.

While writing this thesis, a paper [19] has been published with a more advanced and tested p-value determination based on an unbinned log-likelihood ratio test. The calculation is not tailored to a specific effective volume of the ORCA detector as in this thesis, but thus far results are consistent.

To accurately account for the angle between muon and neutrino, an empirical smearing based on simulated data was developped within the scope of this thesis. The assumption for this type of smearing is that the neutrino direction will be reconstructed from the muon direction. The distribution of the space angle between muon and neutrino obtained from the used data set may be checked with simulated data from a different MC generator.

The three main parts of this thesis – the calculation of neutrino rates, smearing with different detector resolution models and finally the log-likelihood ratio estimator for p-value calculation to estimate the exposure needed for 5σ discrimination – form a simulation chain. This chain may serve as a tool to probe the effects of new assumptions about the inputs for flux calculation or reconstruction strategies. The capability of ORCA to measure the MH hierarchy with an alternated input parameter can be readily estimated using the code developped for this thesis.

References

[1] Carlo Giunti and Chung W. Kim. Fundamentals of Neutrino Physics and Astrophysics. 2007.

[2] Norbert Schmitz. *Neutrinophysik*. Teubner, Stuttgart, 1997.

[3] Particle Data Group. Review of particle physics. *Phys. Rev. D*, 86:010001, 2012. URL `http://link.aps.org/doi/10.1103/PhysRevD.86.010001`.

[4] A. Yu. Smirnov. The MSW effect and solar neutrinos. 2003, hep-ph/0305106.

[5] URL http://upload.wikimedia.org/wikipedia/commons/1/17/NeutrinoHierarchy.svg, March 2013.

[6] F.P. An et al. Observation of electron-antineutrino disappearance at Daya Bay. *Phys.Rev.Lett.*, 108:171803, 2012, 1203.1669.

[7] J.K. Ahn et al. Observation of Reactor Electron Antineutrino Disappearance in the RENO Experiment. *Phys.Rev.Lett.*, 108:191802, 2012, 1204.0626.

[8] E. Kh. Akhmedov, Soebur Razzaque, and A. Yu. Smirnov. Mass hierarchy, 2-3 mixing and CP-phase with Huge Atmospheric Neutrino Detectors. 2012, 1205.7071.

[9] S. Adrian-Martinez et al. Measurement of Atmospheric Neutrino Oscillations with the ANTARES Neutrino Telescope. *Phys.Lett.*, B714:224–230, 2012, 1206.0645.

[10] L. Wolfenstein. Neutrino oscillations in matter. *Phys. Rev. D*, 17:2369–2374, May 1978. URL `http://link.aps.org/doi/10.1103/PhysRevD.17.2369`.

[11] S.P. Mikheev and A. Yu. Smirnov. Resonance Amplification of Oscillations in Matter and Spectroscopy of Solar Neutrinos. *Sov.J.Nucl.Phys.*, 42:913–917, 1985.

[12] Adam M. Dziewonski and Don L. Anderson. Preliminary reference Earth model. *Phys. Earth and Planet. Int.*, 25(4):297–356, 1981.

[13] E K Akhmedov. Parametric resonance in neutrino oscillations in matter. *Pramana - J. Phys.*, 54(hep-ph/9907435. FISIST-99-12-CFIF):47–63, 2000.

[14] The Fermi-LAT Collaboration. Detection of the characteristic pion-decay signature in supernova remnants. 2013, arXiv/1302.3307.

[15] T.K. Gaisser and M. Honda. Flux of atmospheric neutrinos. *Ann.Rev.Nucl.Part.Sci.*, 52:153–199, 2002, hep-ph/0203272.

[16] M. Honda, T. Kajita, K. Kasahara, and S. Midorikawa. Improvement of low energy atmospheric neutrino flux calculation using the JAM nuclear interaction model. *Phys.Rev.*, D83:123001, 2011, 1102.2688.

[17] G.D. Barr, T.K. Gaisser, P. Lipari, Simon Robbins, and T. Stanev. A Three - dimensional calculation of atmospheric neutrinos. *Phys.Rev.*, D70:023006, 2004, astro-ph/0403630.

[18] G. Battistoni, A. Ferrari, T. Montaruli, and P.R. Sala. The FLUKA atmospheric neutrino flux calculation. *Astropart.Phys.*, 19:269–290, 2003, hep-ph/0207035.

[19] D. Franco, C. Jollet, A. Kouchner, V. Kulikovskiy, A. Meregaglia, et al. Mass hierarchy discrimination with atmospheric neutrinos in large volume ice/water Cherenkov detectors. 2013, 1301.4332.

[20] URL http://www.icrr.u-tokyo.ac.jp/~mhonda/nflx2011/index.html, March 2013.

[21] Morihiro Honda. Private communication.

[22] Dominik Stransky. Private communication.

[23] G.L. Fogli, E. Lisi, A. Marrone, D. Montanino, A. Palazzo, et al. Global analysis of neutrino masses, mixings and phases: entering the era of leptonic CP violation searches. *Phys.Rev.*, D86:013012, 2012, 1205.5254.

[24] Y. S. Tsai. Pair production and bremsstrahlung of charged leptons. *Rev. Mod. Phys.*, 46:815–851, 1974.

[25] J. A. Formaggio and G. P. Zeller. From ev to Eev: Neutrino cross sections across energy scales. *Rev. Mod. Phys.*, 84:1307–1341, 2012. URL `http://link.aps.org/doi/10.1103/RevModPhys.84.1307`.

[26] URL www.km3net.org, March 2013.

[27] Ivone F. M. Albuquerque and George F. Smoot. Measuring atmospheric neutrino oscillations with neutrino telescopes. 2001, hep-ph/0102078.

[28] Jannik Hofestädt. Private communication.

[29] David J.L. Bailey. *Monte Carlo tools and analysis methods for understanding the ANTARES experiment and predicting its sensitivity to Dark Matter.* PhD thesis, University of Oxford, Oxford, United Kingdom, 2002.

[30] T. K. Gaisser. *Cosmic Rays And Particle Physics.* Cambridge University Press, 1990.

[31] William M. Smart. *Textbook on Spherical Astronomy, 6th ed.* Cambridge University Press, Cambridge, UK, 1960.

[32] R. Gandhi, C. Quigg, M. Hall Reno, and I. Sarcevic. Ultra-high energy neutrino interactions. *Astroparticle Physics*, 5(2):81–110, 1996.

[33] Hans Otto Georgii, Euthecia Hancewicz, Loretta Heurer, Diana Metsisto, and Cynthia L Tuttle. *Stochastik: Einführung in die Wahrscheinlichkeitstheorie und Statistik*. De Gruyter, Berlin, 2004.

[34] J. Neyman and E. S. Pearson. On the problem of the most efficient tests of statistical hypotheses. *Philosophical Transactions of the Royal Society of London. Series A, Containing Papers of a Mathematical or Physical Character*, 231:289–337, 1933. ISSN 02643952. URL `http://www.jstor.org/stable/91247`.

Appendix

A. Muon track length

The muon range used in this work is $4.25\,\mathrm{m} \cdot E_\nu/\mathrm{GeV}$. This is a good approximation for $1\,\mathrm{GeV} \leq E_\nu \leq 20\,\mathrm{GeV}$ as can be seen from the track lengths of simulated data in Fig. 25.

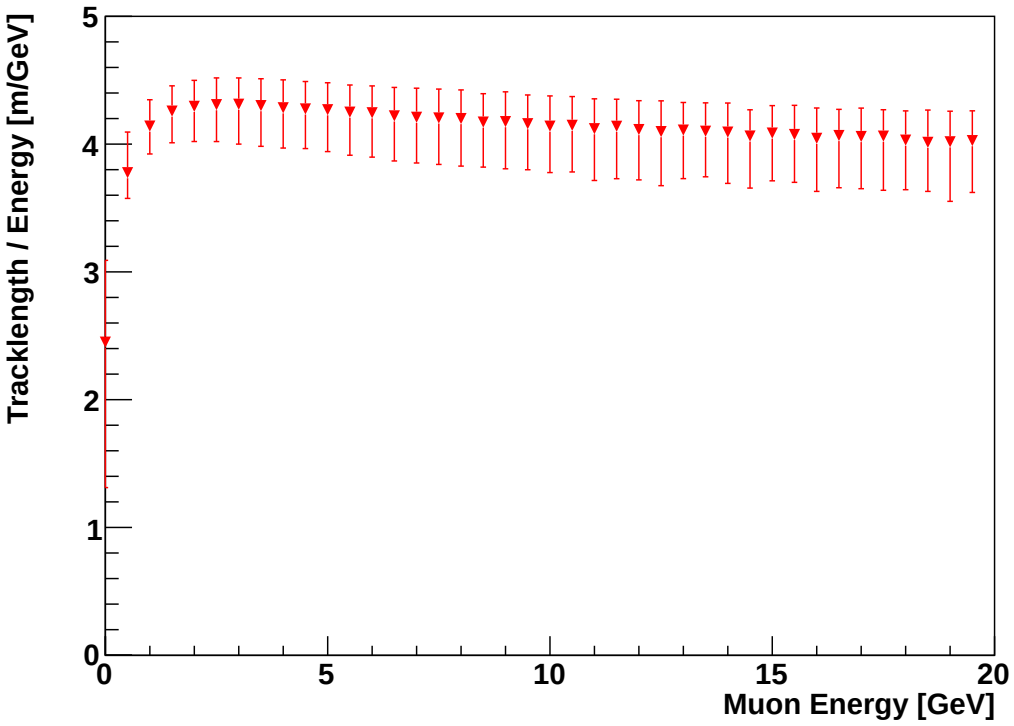

Figure 25: Energy dependent mean muon range. The "error bars" indicate 15% and 85% quantiles. Figure from [28].

B. Other oscillation probabilities for oscillations to muon-type neutrinos

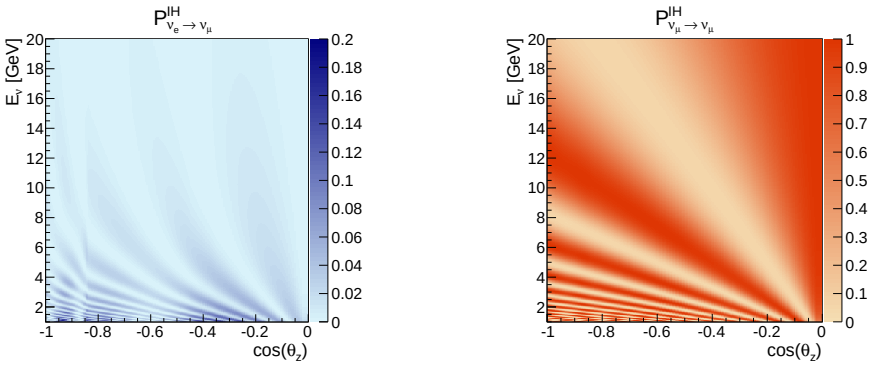

Figure 26: Appearance and survival probabilities for ν_μ , IH assumed

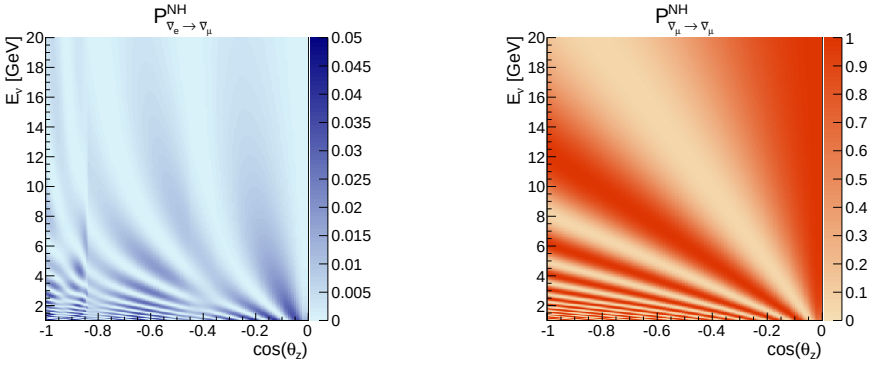

Figure 27: Appearance and survival probabilities for $\overline{\nu}_\mu$, NH assumed

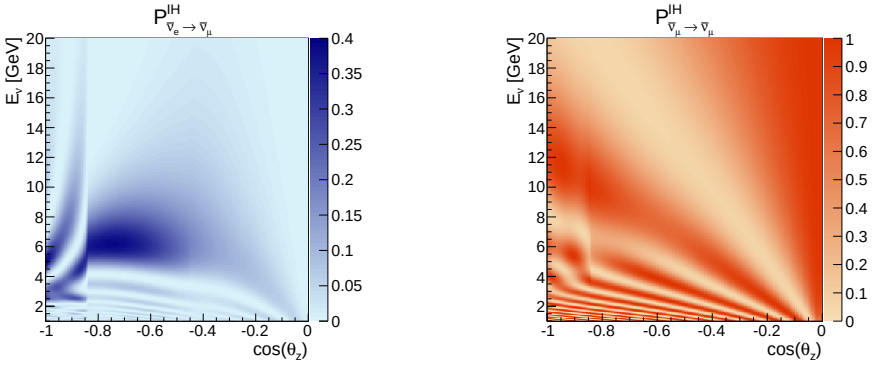

Figure 28: Appearance and survival probabilities for $\overline{\nu}_\mu$, IH assumed

C. Bjorken y distribution of simulated data for different energies

In the energy range below 5 GeV the influence of quasi-elastic scattering and resonance production is visible in the Bjorken y distribution. Deep inelastic scattering dominates above 5 GeV and the Bjorken y distribution is steady as can be seen from Fig. 29.

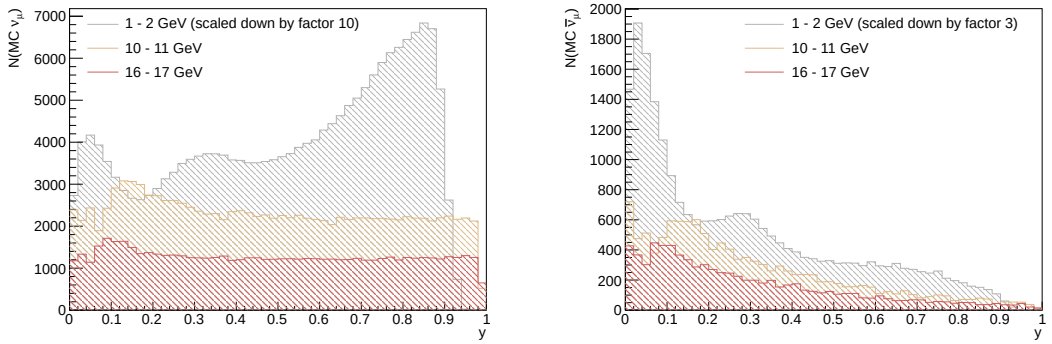

Figure 29: Bjorken y distribution of simulated data for ν_μ and $\overline{\nu}_\mu$ and different neutrino energies. N(MC ν_μ) is the number of neutrino events simulated with the GENHEN [29] Monte Carlo generator.

D. p-values after kinematic smearing with θ_{RMS}

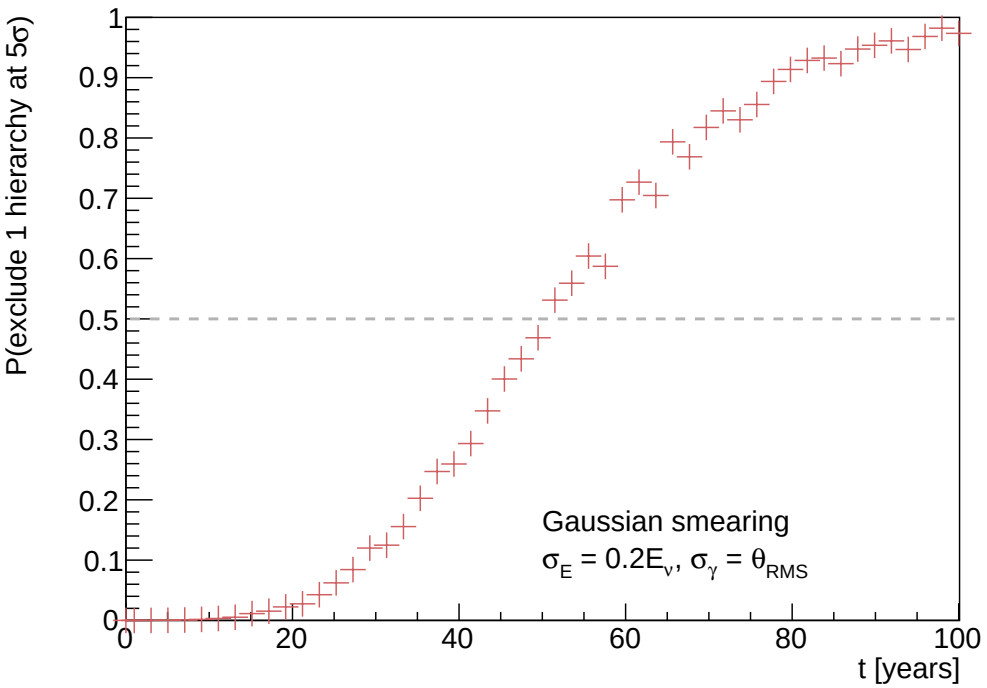

Figure 30: P-values for Gaussian smearing with $\sigma_E = 0.2E\nu$ and $\sigma_\gamma = \theta_{\mathrm{RMS}}$

Statutory Declaration

I declare that I have developed and written the enclosed thesis entirely by myself and have not used sources or means without declaration in the text. Any thoughts or quotations which were inferred from these sources are cleary marked as such. This thesis was not submitted in the same or in a substantially smiliar version, not even partially, to any other authority to achieve an academic grading and was not published elsewhere.

Steffen Hallmann Erlangen, 04/04/2013

Acknowledgements

An dieser Stelle möchte ich mich kurz bei allen bedanken, die mich beim Anfertigen dieser Arbeit unterstützt haben. Insbesondere bedanke ich mich bei

- Frau Professor Anton für die Vergabe eines so aktuellen und interessanten Themas
- den ORCAs Dominik Stransky, Jannik Hofestädt und Thomas Eberl für ihre zahlreichen und sehr hilfreichen Ratschläge, sowie Beiträge zur Berechnung der Neutrinoraten
- meinen Zimmergenossen für die nette Aufnahme und schnellen Ratschläge bei programmiertechnischen Fragen
- ganz besonders bei meinem Betreuer Jürgen Hößl, der stets ein offenes Ohr und oft auch noch eine Tasse Kaffee für mich hatte.